



Supernova 2018cuf: A Type IIP Supernova with a Slow Fall from Plateau

Yize Dong (董一泽)¹, S. Valenti¹, K. A. Bostroem¹, D. J. Sand², Jennifer E. Andrews², L. Galbany³,
 Saurabh W. Jha⁴, Youssef Eweis^{4,5}, Lindsey Kwok⁴, E. Y. Hsiao⁶, Scott Davis¹, Peter J. Brown⁷, H. Kuncarayakti^{8,9},
 Keiichi Maeda^{10,11}, Jeonghee Rho¹², R. C. Amaro², J. P. Anderson¹³, Iair Arcavi^{14,15}, Jamison Burke^{16,17},
 Raya Dastidar^{18,19}, Gastón Folatelli^{11,20,21}, Joshua Haislip²², Daichi Hiramatsu^{16,17}, Griffin Hosseinzadeh²³,
 D. Andrew Howell^{16,17}, J. Jencson², Vladimir Kouprianov²², M. Lundquist², J. D. Lyman²⁴, Curtis McCully^{16,17},
 Kuntal Misra¹⁸, Daniel E. Reichart²², S. F. Sánchez²⁵, Nathan Smith², Xiaofeng Wang²⁶, Lingzhi Wang^{27,28}, and
 S. Wyatt²

¹ Department of Physics and Astronomy, University of California, 1 Shields Avenue, Davis, CA 95616-5270, USA; yizdong@ucdavis.edu

² Steward Observatory, University of Arizona, 933 North Cherry Avenue, Room N204, Tucson, AZ 85721-0065, USA

³ Departamento de Física Teórica y del Cosmos, Universidad de Granada, E-18071 Granada, Spain

⁴ Department of Physics and Astronomy, Rutgers, the State University of New Jersey, 136 Frelinghuysen Road, Piscataway, NJ 08854, USA

⁵ Department of Physics and Astronomy, Iowa State University, Ames, IA 50011, USA

⁶ Department of Physics, Florida State University, 77 Chieftan Way, Tallahassee, FL 32306, USA

⁷ Department of Physics and Astronomy, Texas A&M University, 4242 TAMU, College Station, TX 77843, USA

⁸ Tuorla Observatory, Department of Physics and Astronomy, University of Turku, Turku FI-20014, Finland

⁹ Finnish Centre for Astronomy with ESO (FINCA), University of Turku, Turku FI-20014, Finland

¹⁰ Department of Astronomy, Graduate School of Science, Kyoto University, Sakyo-ku, Kyoto 606-8502, Japan

¹¹ Kavli Institute for the Physics and Mathematics of the Universe (WPI), The University of Tokyo, 5-1-5 Kashiwanoha, Kashiwa, Chiba 277-8583, Japan

¹² SETI Institute, 189 North Bernardo Avenue, Mountain View, CA 94043, USA

¹³ European Southern Observatory, Alonso de Córdova 3107, Vitacura, Casilla 190001, Santiago, Chile

¹⁴ The School of Physics and Astronomy, Tel Aviv University, Tel Aviv 69978, Israel

¹⁵ CIFAR Azrieli Global Scholars Program, CIFAR, Toronto, Canada

¹⁶ Department of Physics, University of California, Santa Barbara, CA 93106-9530, USA

¹⁷ Las Cumbres Observatory, 6740 Cortona Drive, Suite 102, Goleta, CA 93117-5575, USA

¹⁸ Aryabhata Research Institute of Observational Sciences, Manora Peak, Nainital 263 001, India

¹⁹ Department of Physics & Astrophysics, University of Delhi, Delhi-110 007, India

²⁰ Facultad de Ciencias Astronómicas y Geofísicas, Universidad Nacional de La Plata, Paseo del Bosque S/N, B1900FWA La Plata, Argentina

²¹ Instituto de Astrofísica de La Plata (IALP), CONICET, Argentina

²² Department of Physics and Astronomy, University of North Carolina at Chapel Hill, Chapel Hill, NC 27599, USA

²³ Center for Astrophysics|Harvard & Smithsonian, 60 Garden Street, Cambridge, MA 02138-1516, USA

²⁴ Department of Physics, University of Warwick, Coventry CV4 7AL, UK

²⁵ Instituto de Astronomía, Universidad Nacional Autónoma de México Circuito Exterior, Ciudad Universitaria, Ciudad de México 04510, Mexico

²⁶ Physics Department and Tsinghua Center for Astrophysics (THCA), Tsinghua University, Beijing, 100084, People's Republic of China

²⁷ CAS Key Laboratory of Optical Astronomy, National Astronomical Observatories, Chinese Academy of Sciences, Beijing 100101, People's Republic of China

²⁸ Chinese Academy of Sciences South America Center for Astronomy, National Astronomical Observatories, CAS, Beijing 100101, People's Republic of China

Received 2020 July 22; revised 2020 October 16; accepted 2020 October 20; published 2021 January 7

Abstract

We present multiband photometry and spectroscopy of SN 2018cuf, a Type IIP (“P” for plateau) supernova (SN) discovered by the Distance Less Than 40 Mpc Survey within 24 hr of explosion. SN 2018cuf appears to be a typical SN IIP, with an absolute V-band magnitude of -16.73 ± 0.32 at maximum and a decline rate of 0.21 ± 0.05 mag/50 days during the plateau phase. The distance of the object was constrained to be 41.8 ± 5.7 Mpc by using the expanding photosphere method. We used spectroscopic and photometric observations from the first year after the explosion to constrain the progenitor of SN 2018cuf using both hydrodynamic light-curve modeling and late-time spectroscopic modeling. The progenitor of SN 2018cuf was most likely a red supergiant of about $14.5 M_{\odot}$ that produced $0.04 \pm 0.01 M_{\odot}$ ^{56}Ni during the explosion. We also found $\sim 0.07 M_{\odot}$ of circumstellar material (CSM) around the progenitor is needed to fit the early light curves, where the CSM may originate from presupernova outbursts. During the plateau phase, high-velocity features at $\sim 11,000 \text{ km s}^{-1}$ were detected in both the optical and near-infrared spectra, supporting the possibility that the ejecta were interacting with some CSM. A very shallow slope during the postplateau phase was also observed, and it is likely due to a low degree of nickel mixing or the relatively high nickel mass in the SN.

Unified Astronomy Thesaurus concepts: Core-collapse supernovae (304); Type II supernovae (1731)

Supporting material: machine-readable table

1. Introduction

Type II supernovae (SNe), the most common type of core-collapse supernova, originate from the collapse of stars more massive than $\sim 8 M_{\odot}$. In the Type IIP subclass, the SN experiences a period of nearly constant luminosity for ~ 2 – 3 months after maximum as the hydrogen envelope recombines.

This is then followed by a rapid drop from the plateau, where the light curve becomes dominated by radioactive decay and the SN enters the nebular phase.

From pre-explosion imaging at the location of the explosions, the progenitors of SNe IIP have been mostly attributed to red supergiants (RSGs) with initial masses of ~ 8 – $17 M_{\odot}$.

(van Dyk et al. 2003; Smartt et al. 2009; Smartt 2015). However, evolutionary codes predict that the progenitors of SNe IIP can have masses up to $30 M_{\odot}$ (e.g., Heger et al. 2003; Ekström et al. 2012). This discrepancy between observations and theory has been dubbed the “RSG problem.” This problem has been discussed by many authors (e.g., Kochanek et al. 2012; Walmswell & Eldridge 2012; Horiuchi et al. 2014; Davies & Beasor 2018, 2020) and remains an open question. An alternative method that is widely used to estimate the progenitor masses of SNe II is the hydrodynamic modeling of SN light curves (e.g., Utrobin & Chugai 2015, 2017; Morozova et al. 2017, 2018; Paxton et al. 2018; Goldberg et al. 2019; Martinez & Bersten 2019). Through comparing observed light curves with model light curves, many progenitor properties, such as mass, radius, and explosion energy, could be determined. Another approach to estimate the progenitor mass is nebular spectral modeling (Jerkstrand et al. 2012, 2014). Here the structure and composition of the ejecta can be constrained, and the intensity of the [O I] $\lambda\lambda 6300, 6363$ doublet can be used to derive the progenitor mass.

These various methods sometimes do not predict a consistent progenitor mass for a given SN, so continued observational and theoretical work is necessary for these different techniques to converge (Jerkstrand et al. 2014; Davies & Beasor 2018; Morozova et al. 2018). The progenitor mass distribution inferred from hydrodynamic modeling is generally greater than the observed mass range from direct imaging, mitigating the RSG problem (Morozova et al. 2018, although see Martinez et al. 2020, where consistent masses are obtained between hydrodynamical modeling and other methods). On the other hand, Jerkstrand et al. (2014) found from nebular spectral modeling that there is no evidence yet that the progenitor of an observed SN II is more massive than $20 M_{\odot}$, supporting the presence of the RSG problem. However, some recent SN studies have found more massive progenitors based on nebular spectral modeling (Anderson et al. 2018; Bose et al. 2020). It is important to note that the sample of SNe that have been studied by these two modeling techniques is small. Increasing the sample size is necessary to fully examine the existence of the RSG problem.

For this purpose, observations both in the first few days after explosion and during the nebular phase (~ 300 – 500 days after explosion) are required. Unfortunately rapid discovery and follow-up of SNe is still rare, and often SNe IIP are not followed out to the nebular phase when larger telescopes are needed. Thankfully, modern SN surveys such as the All Sky Automated Survey for Supernovae (Shappee et al. 2014; Kochanek et al. 2017), the Zwicky Transient Facility (Bellm et al. 2019), the Asteroid Terrestrial-Impact Last Alert System (Tonry 2011; Smith et al. 2020), and the Distance Less Than 40 Mpc Survey (DLT40; Tartaglia et al. 2018) are now able to discover SNe within hours of explosion and use dedicated facilities for follow-up, such as the Las Cumbres Observatory (Brown et al. 2013). The very early light curves of core-collapse SNe provided by these surveys can be used to constrain the progenitor radius (and potentially the envelope structure), ejected mass, and kinetic energy of the explosion (e.g., Rabinak & Waxman 2011; Arcavi et al. 2017; Piro et al. 2017; Sapir & Waxman 2017; Bersten et al. 2018, for selected theoretical and observational results).

In this paper, we present optical and infrared photometry and spectroscopy of SN 2018cuf, an SN II discovered within 30 hr

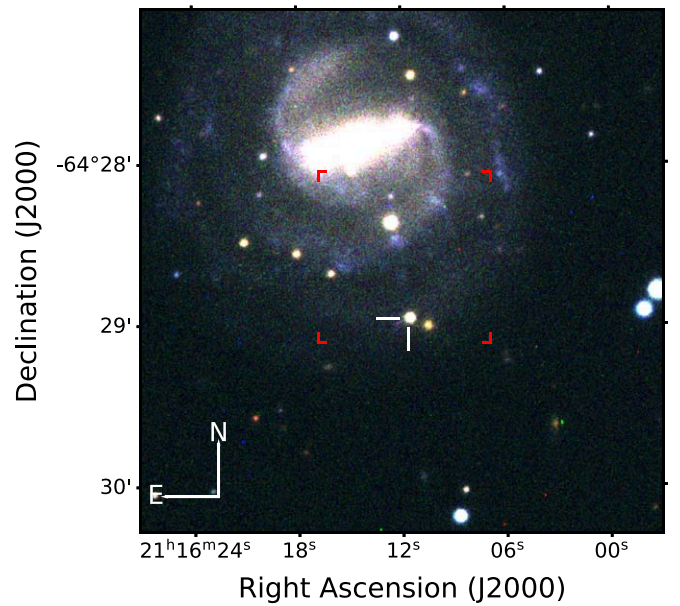


Figure 1. RGB image of SN 2018cuf (indicated by white tick marks) in IC 5092 obtained with the Las Cumbres Observatory on 2018 September 17. The red markers delineate the Multi Unit Spectroscopic Explorer (MUSE) field of view, as described in Section 3.2.

of explosion by the DLT40 survey and densely monitored within the Global Supernova Project (GSP)²⁹ for over 340 days. This paper is organized as follows: the observations of SN 2018cuf are presented in Section 2, while the reddening and host galaxy properties are presented in Section 3. Further observational properties, such as the distance and explosion epoch, are constrained in Section 4. In Section 5 we analyze the light curves and in Section 6 the spectroscopic evolution is described. We constrain the nickel mass and progenitor mass using our extensive observational data set in Section 7, and finally we present our conclusions in Section 8.

2. Observations

SN 2018cuf was discovered at R.A.(2000) = $21^{\text{h}}16^{\text{m}}11^{\text{s}}58$, decl.(2000) = $-64^{\circ}28'57''30$ in the nearby SBc galaxy IC 5092 (see Figure 1) on 2018 June 23 (Valenti et al. 2018; JD 2,458,292.86093, $r = 17.4$) during the course of the DLT40 SN search (Tartaglia et al. 2018), utilizing the 0.4 m PROMPT5 telescope (Reichert et al. 2005) at the Cerro Tololo Inter-American Observatory (CTIO). A nondetection ~ 24 hr earlier (JD 2,458,291.74456, $r \lesssim 19.4$) strongly constrains the explosion epoch (see Figure 2). The 1 day cadence of the DLT40 SN search is designed to discover ~ 10 nearby SNe (< 40 Mpc) per year within 24 hr of explosion. The mechanics of the survey have been described elsewhere (Yang et al. 2017; Tartaglia et al. 2018; Yang et al. 2019), along with the recent addition of a second telescope in Australia (for an effective ~ 12 hr cadence), improvements to our machine-learning search algorithm, and the fast telescope triggering infrastructure (Bostroem et al. 2020).

Shortly after discovery, we triggered high-cadence observations with the worldwide network of robotic telescopes associated with the Las Cumbres Observatory and the Neil Gehrels Swift Observatory (Gehrels et al. 2004). The

²⁹ GSP is a key project at Las Cumbres Observatory.

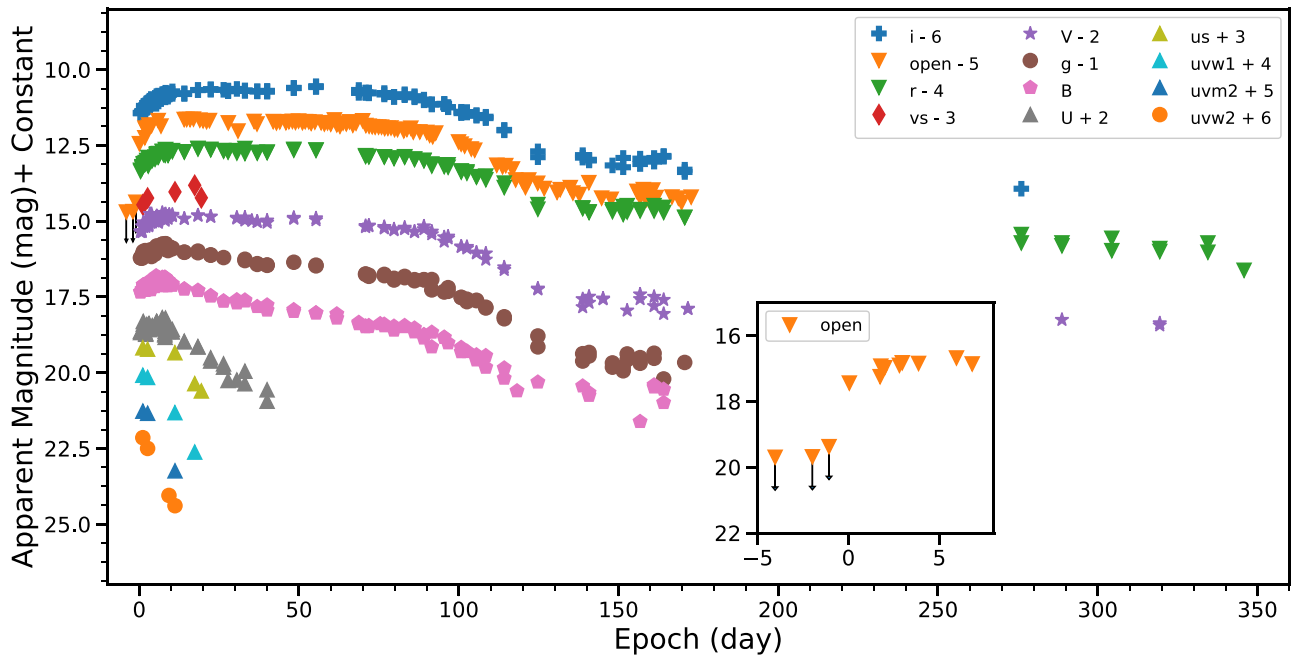


Figure 2. Multiband light curves for SN 2018cuf with respect to the epoch of explosion. An *Open* filter is used by the PROMPT5 0.4 m telescope and is calibrated to the *r* band. The inset is a zoom on the *Open* filter illustrating the DLT40 detection limit ~ 1 day before discovery.

photometric data from the Las Cumbres Observatory were reduced using the PyRAF-based photometric reduction pipeline LCOGTSNPIPE (Valenti et al. 2016). This pipeline uses a low-order polynomial fit to remove the background and calculates instrumental magnitudes using a standard point-spread function (PSF) fitting technique. Apparent magnitudes were calibrated using the APASS (*B*, *V*, *g*, *r*, *i*) and Landolt (*U*) catalogs. Background contamination was removed by subtracting a reference image, and photometry was extracted from the subtracted images. The Swift UVOT images were reduced using the method described in Brown et al. (2009) using the updated zero-points of Breeveld et al. (2011). The multiband light curves are shown in Figure 2 and the magnitudes are listed in Table A1. The Swift photometry is available in the Swift Optical Ultraviolet Supernova Archive (Brown et al. 2014).

The spectroscopic observations of SN 2018cuf started on 2018 June 24 (~ 1 day after discovery) and continued through 2019 October 19. A number of optical spectra were collected by the Southern African Large Telescope (SALT), including the first classification spectrum, which classified SN 2018cuf as a young SN Type II (Jha 2018). In addition, many low-dispersion optical spectra were obtained by the FLOYDS spectrograph (Brown et al. 2013) on the 2 m Faulkes Telescope South in Australia, and these spectra were reduced following standard procedures using the FLOYDS pipeline (Valenti et al. 2014). One optical spectrum was taken with the GMOS instrument (Hook et al. 2004; Gimeno et al. 2016) at the Gemini South telescope on 2018 June 24 05:33:32 UT, under program GS-2018A-Q-116. GMOS was used in longslit spectroscopy mode with the B600 grating, with a total exposure time of 750 s, and the spectrum was reduced by using the IRAF Gemini package. However, this spectrum had a very low signal-to-noise ratio, so we did not use it for analysis. We also used FORS2 (Appenzeller et al. 1998) at the Very Large Telescope (VLT) with the GRIS_150I grism and GG435 blocking filter to observe SN 2018cuf on 2018 December 14 00:48:30 UT, as part of the FOSSIL program (H. Kuncarayakti

et al. 2020, in preparation). The total exposure time was 2700 s. The data were reduced using EsoReflex software (Freudling et al. 2013). The low-dispersion optical spectra are shown in Figure 3. There was also one high-resolution optical spectrum taken by the Magellan Inamori Kyocera Echelle instrument (MIKE; Bernstein et al. 2003) on the Magellan Clay Telescope (Figure 4), and the data were reduced using the latest version of the MIKE pipeline³⁰ (written by D. Kelson).

Near-infrared (NIR) spectra were taken with the FLAMINGOS-2 instrument (F2; Eikenberry et al. 2006) at Gemini South Observatory and the Folded-port Infrared Echellette instrument (FIRE; Simcoe et al. 2013) on the Magellan Baade telescope. The Magellan FIRE spectra were obtained in high-throughput prism mode with a $0''.6$ slit, giving continuous wavelength coverage from 0.8 to $2.5 \mu\text{m}$. For the Gemini South F2 spectra, we observed with the JH grism and $0''.72$ slit in place, yielding a wavelength range of 1.0– $1.8 \mu\text{m}$. For both the FIRE and F2 data, observations were taken with a standard ABBA pattern for sky subtraction, and an A0V star was observed adjacent to the science exposures for both telluric corrections and flux calibration. Data for both instruments were reduced in a standard manner as described in Hsiao et al. (2019), and we refer the reader there for the details. The NIR spectra are presented in Figure 5. All the spectroscopic observations are listed in Table A2 and will be available on WISerEP (Yaron & Gal-Yam 2012).³¹

3. Reddening and Host Properties

3.1. Reddening

The Milky Way line-of-sight reddening toward SN 2018cuf is $E(B-V)_{\text{MW}} = 0.0273 \pm 0.0003$ mag (Schlafly & Finkbeiner 2011). This low extinction value is also supported by the lack of NaID lines from the Milky Way in the Magellan/MIKE

³⁰ <https://code.obs.carnegiescience.edu/mike/>

³¹ <http://www.weizmann.ac.il>

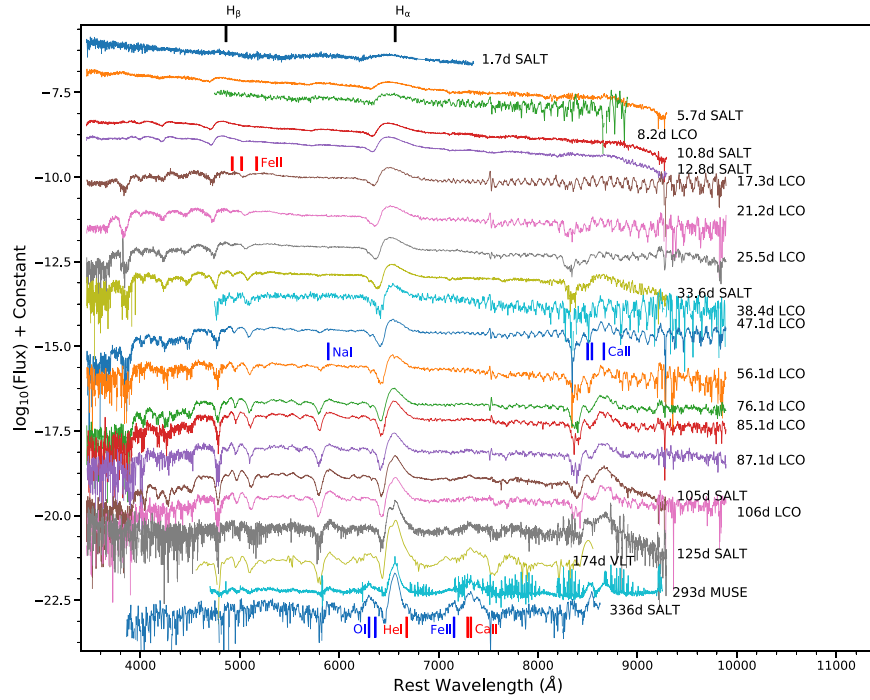


Figure 3. The optical spectroscopic evolution of SN 2018cuf from 2 to 336 days after explosion.

spectrum taken on 2018 July 12 and shown in Figure 3. The equivalent width (EW) of the NaID line is often used to estimate the SN reddening with the assumption that it is a good tracer of gas and dust (Munari & Zwitter 1997; Poznanski et al. 2012). The measured EWs of the host galaxy NaID $\lambda 5890$ (D_2) and NaID $\lambda 5896$ (D_1) are 0.677 \AA and 0.649 \AA , respectively. The intensity ratio of D_2 to D_1 ($D_2/D_1 \sim 1$) is far from the typical value of 2 we usually observe (Munari & Zwitter 1997), suggesting that at least D_2 may be saturated (see Figure 3). Using only D_1 , we found a host galaxy extinction of $E(B-V)_{\text{host}} = 0.699 \pm 0.17 \text{ mag}$.

Phillips et al. (2013) suggested that the most accurate predictor of extinction is the diffuse interstellar band absorption feature at 5780 \AA . However, this feature is not clearly present in our high-resolution spectrum of SN 2018cuf, suggesting the host galaxy extinction is low, which is inconsistent with the high host reddening derived from NaID lines. Munari & Zwitter (1997) found that $[\text{K I}] \lambda 7699$ can be a better reddening indicator if NaID lines are saturated, so we decided to use this line to estimate the reddening from the host galaxy. The EW of $[\text{K I}] \lambda 7699$ was measured to be 0.03 \AA , which corresponds to a host galaxy extinction of $E(B-V)_{\text{host}} = 0.11 \pm 0.01 \text{ mag}$ (Munari & Zwitter 1997). As a sanity check, we also compared the dereddened $B - V$ color evolution of SN 2018cuf to a sample of similar SNe II with published reddening estimates. This includes SN 1993A (Anderson et al. 2014; Galbany et al. 2016b), SN 1999gi (Leonard et al. 2002b), SN 2003iq (Faran et al. 2014), SN 2003bn (Anderson et al. 2014; Galbany et al. 2016b), SN 2003ef (Anderson et al. 2014; Galbany et al. 2016b), SN 2003T (Anderson et al. 2014; Galbany et al. 2016b), SN 2009ib (Takáts et al. 2015), and SN 2012A (Tomasella et al. 2013), as is shown in Figure 6. SN 2018cuf has a similar V -band light-curve slope after maximum with these selected SNe. de Jaeger et al. (2018) found that the color evolution of SNe is related to the slope of the V -band light curve, so these selected SNe should have consistent colors with

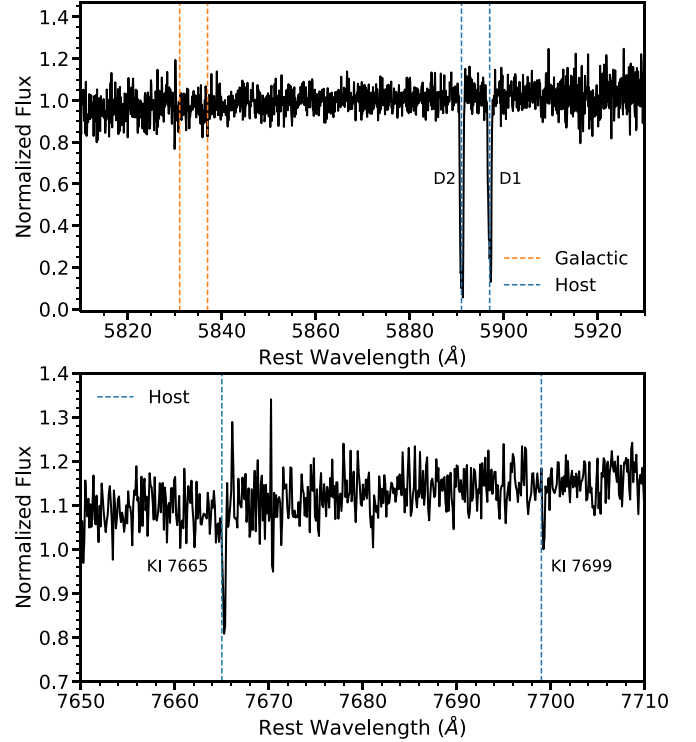


Figure 4. An echelle spectrum with a resolution of $R \simeq 40,000$ from Magellan/MIKE taken on +18.7 days showing the region around the galactic (dashed orange lines) and host (dashed blue lines) NaID lines (top) and the host KI lines (bottom).

SN 2018cuf after dereddening. We found that an $E(B-V)_{\text{host}} \approx 0.11 \text{ mag}$ gives us a consistent color evolution with the other objects. Therefore throughout this paper we will adopt an $E(B-V)_{\text{tot}} = 0.1373 \pm 0.0103 \text{ mag}$, as well as an $R_V = 3.1$ (Cardelli et al. 1989).

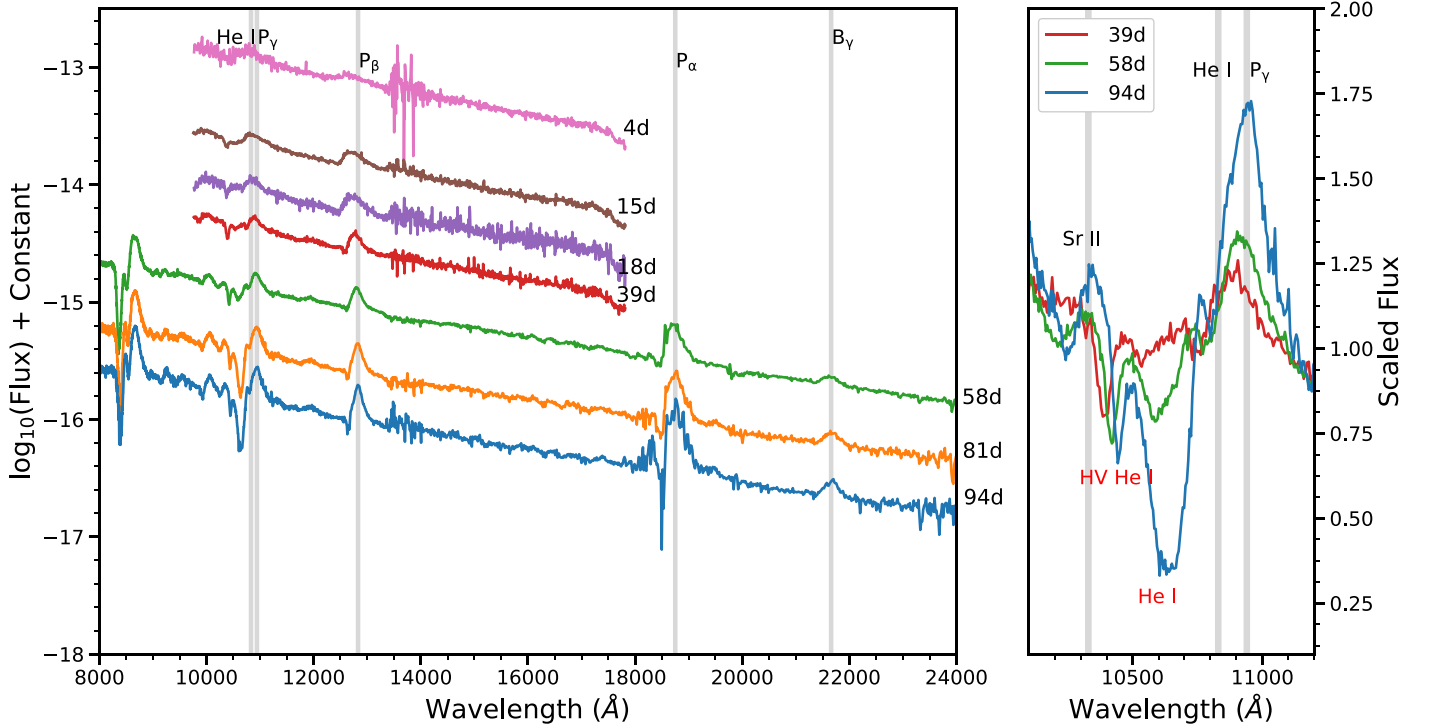


Figure 5. Left: NIR spectra of SN 2018cuf from Gemini+FLAMINGOS-2 and Magellan+FIRE. Right: A zoomed-in version for spectra at day 39, day 58, and day 94. The high-velocity (HV) He I feature and He I absorption are labeled.

The disagreement between host reddening values obtained from the NaID lines and direct color comparisons to similar objects is not a unique problem. Leonard et al. (2002a) found a similar situation for SN 1999em, i.e., the EW of the sodium lines suggested a high reddening for SN 1999em, but a low value was assumed based on color comparisons. Phillips et al. (2013) also found that NaID gives unreasonably high reddening for some of their objects, while the KI line gives a reddening that is consistent with the reddening derived from SN colors.

3.2. Host Properties

MUSE (Bacon et al. 2010) integral field unit observations of IC 5092 were taken on 2019 April 12, as a part of the All-weather MUSE Supernova Integral-field Nearby Galaxies (Galbany et al. 2016a) survey. MUSE is mounted to the 8.2 m Yepun UT4 Very Large Telescope, with a field of view of $1' \times 1'$ and $0''.2 \times 0''.2$ spatial elements, small enough to sample the PSF. See Figure 1 for an outline of the MUSE footprint. The spectral coverage is from 4750 to 9300 Å, with a spectral resolution that ranges from $R \simeq 3500$ in the blue end to $\simeq 1700$ in the red end. Four 580 s exposures (2320 s total exposure time), rotating 90° between frames, were taken centered on the southwest side of the galaxy, which covered the SN position and its environment.

We extracted a $3''.6$ aperture spectrum centered at the SN position (corresponding to an ~ 800 pc diameter) to study the properties of the environment. The resulting spectrum is shown in Figure 4. MUSE observations were performed 293 days after SN 2018cuf's explosion, and some SN features were still visible in the spectrum, with the most pronounced being a broad Balmer H α emission, in addition to an H II region spectrum with narrow emission lines. To measure the flux of the strongest ionized gas emission lines in that region ([N II] $\lambda 6548$, H α , and [N II] $\lambda 6583$), we excluded the SN

broad component by fitting four Gaussians, three narrow and one broad, simultaneously. The bluer region of the spectrum was not strongly contaminated by SN features, and we fit single Gaussians to measure the narrow H β and [O III] $\lambda 5007$ emission line fluxes from the ionized gas.

An estimate of the reddening can be obtained from the line-of-sight gas column by the ratio of the Balmer lines, assuming a case B recombination (Osterbrock & Ferland 2006) and a theoretical ratio of $H\alpha/H\beta = 2.86$. Our lines present a ratio of 4.54, which corresponds to $E(B-V) = 0.399 \pm 0.021$ mag. This value is not consistent with the reddening estimated from our color comparison (Figure 6) and would make the light curves of SN 2018cuf significantly bluer and brighter than those of similar SNe II. A possible explanation for this disagreement is that the SN is in front of the H II region and not influenced by the dust, but the MUSE measurement gets the full column of gas.

With the host galaxy reddening-corrected fluxes we estimated the SN environmental oxygen abundance (O/H) by using the N2 and O3N2 calibrators from Pettini & Pagel (2004). We obtained a consistent oxygen abundance of $12+\log(O/H) = 8.71 \pm 0.07$ dex and $12+\log(O/H) = 8.72 \pm 0.08$ dex with the N2 and O3N2 calibrators, respectively, both consistent with solar abundance (Asplund et al. 2009). We used the H α luminosity to estimate the star formation rate (SFR) at the SN location using the expression provided by Kennicutt (1998). We obtained an SFR of $0.0014 \pm 0.0001 M_\odot \text{ yr}^{-1}$ and an SFR intensity of $0.0027 \pm 0.0001 M_\odot \text{ yr}^{-1} \text{ kpc}^{-2}$. To understand where SN 2018cuf stands in the SNe II group, we compared the values we derived above with the host properties of all SNe II in the PMAS/PPak Integral-field Supernova Hosts Compilation (PISCO) sample (Galbany et al. 2018).³² The

³² Observations are updated to 2020 June.

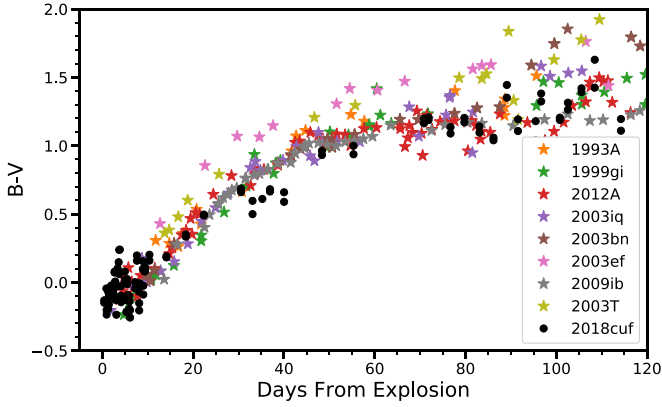


Figure 6. Color evolution of SN 2018cuf, after correcting for a total color excess of $E(B - V)_{\text{MW}} = 0.1373$ mag. We also plot a sample of SNe II with published reddening estimates (see Section 3 for details), and SN 2018cuf shows a color evolution similar to that of the other objects.

average host oxygen abundance and SFR intensity for all PISCO Type II hosts are $12 + \log(\text{O}/\text{H}) = 8.53 \pm 0.062$ dex and $0.013 \pm 0.0014 M_{\odot} \text{ yr}^{-1} \text{ kpc}^{-2}$, respectively, suggesting that the region around SN 2018cuf has a higher oxygen abundance but a lower SFR intensity than the average of SNe II.

4. Observational Properties

4.1. Distance

The distance to IC 5092 is not well constrained since it has only been measured using the Tully–Fisher relation (Mathewson et al. 1992; Willick et al. 1997) to be 32.0 ± 5.8 Mpc. While the Tully–Fisher relation can be used to measure distances to most spiral galaxies, the intrinsic scatter hinders the accuracy of the measurement for a single galaxy (Czerny et al. 2018). One commonly used approach to independently measure distances to SNe II is the expanding photosphere method (EPM), although it requires the object to have well-sampled light curves and spectra. The EPM was first developed by Kirshner & Kwan (1974) to calculate the distance to SNe IIP based on the Baade (1926) method. Assuming that the photosphere is expanding freely and spherically, we can obtain the distance from the linear relation between the angular radius and the expanding velocity of the photosphere using the function

$$t = D \left(\frac{\theta}{v_{\text{phot}}} \right) + t_0 \quad (1)$$

where D is the distance, t_0 is the explosion epoch, θ is the radius of the photosphere (in angular units), and v_{phot} is the velocity of the photosphere. Assuming that the photosphere radiates as a dilute blackbody, we combined the multiband photometry to simultaneously derive the angular size (θ) and color temperature (T_c) by minimizing the equation

$$\epsilon = \sum_{\nu \in S} \{m_{\nu} + 5 \log[\theta \xi(T_c)] - A_{\nu} - b_{\nu}(T_c)\}^2 \quad (2)$$

where ξ and b_{ν} are the dilution factor and synthetic magnitude, respectively, and both of them can be treated as a function of T_c (Hamuy et al. 2001; Dessart & Hillier 2005), A_{ν} is the reddening, m_{ν} is the observed magnitude, and S is the filter subsets, i.e., {BV}, {BVI}, and {VI}. We estimated the

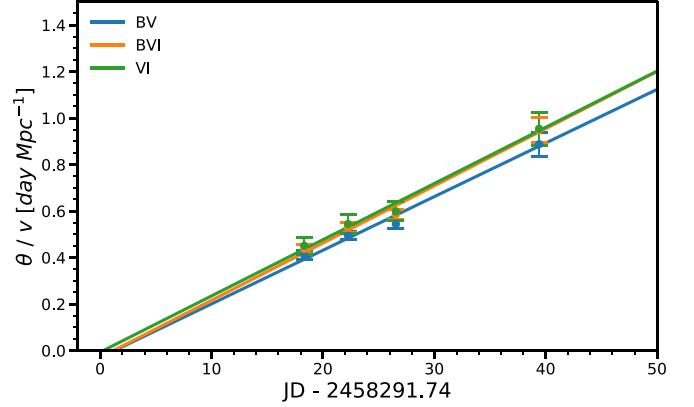


Figure 7. EPM fitting for SN 2018cuf using three filter subsets: {BV}, {BVI}, and {VI}. The derived distances are 43.3 ± 5.8 Mpc, 40.6 ± 5.2 Mpc, and 41.3 ± 7.4 Mpc for the three filter subsets, respectively, and the weighted average is 41.8 ± 5.8 Mpc.

Table 1
The Velocities of [Fe II] $\lambda 5169$ Used in the EPM

Date	[Fe II] $\lambda 5169$ Velocity (km s ⁻¹)
2018-07-10	7641.3 ± 141.8
2018-07-14	6664.1 ± 68.3
2018-07-18	6328.8 ± 79.8
2018-07-31	4311.7 ± 210.1

photospheric velocity by measuring the minimum of the [Fe II] $\lambda 5169$ P Cygni profile. To accurately estimate the error on this measurement and avoid noise-induced local minima, we smoothed the spectra with Savitzky–Golay filters (Savitzky & Golay 1964; Poznanski et al. 2010) with different widths, deriving the photospheric velocity for each width. For our distance measurement we used the mean and standard deviation of these velocity measurements. After ~ 40 days, the relation between θ/v and t was clearly nonlinear (Jones et al. 2009), and for this reason we only used four early spectra with clear [Fe II] $\lambda 5169$ detection and interpolated the photometry data to the corresponding epoch. The measured velocities are listed in Table 1. In order to use the dilution factor derived by Dessart & Hillier (2005), we converted the rp and ip magnitude to I magnitudes by using the equations given by Lupton et al. (2005). The results for the three filter subsets {BV}, {BVI}, and {VI} are presented in Figure 7. From these measurements, we obtained distances of 43.3 ± 5.8 Mpc, 40.6 ± 5.2 Mpc, and 41.3 ± 7.4 Mpc, respectively, and the weighted average was calculated to be 41.8 ± 5.8 Mpc by using the method described in Schmelling (1995). In the rest of the paper, we will adopt this value for the analysis.

4.2. Explosion Epoch

We derived the explosion epoch from the EPM analysis, obtaining similar values from each of the three filter subsets used: JD 2,458,293.04 \pm 2.88 days in {BV}, JD 2,458,292.95 \pm 2.82 days in {BVI}, and JD 2,458,292.02 \pm 4.22 days in {VI}. The weighted average of these measurements is JD 2,458,292.81 \pm 3.08, which we adopt as the explosion epoch throughout

this paper. We note that this is consistent with the tight constraints of the DLT40 survey, which place the explosion epoch between JD 2,458,291.74456 (the last nondetection) and JD 2,458,292.8609 (the first detection, which is just 0.05 d after the estimated explosion epoch).

As an independent check, we also estimated the explosion epoch by matching the spectra of SN 2018cuf with the spectral templates in the Supernova Identification (SNID) code (Blondin & Tonry 2007). This method has been used by Anderson et al. (2014) and Gutiérrez et al. (2017) to constrain the explosion epochs of a sample of SNe II. Gutiérrez et al. (2017) found that with the addition of new spectral templates to the SNID database, the explosion epoch derived from spectral matching may constrain the explosion to within 3.9 days. Following the work of Gutiérrez et al. (2017), we fixed the fitting range in SNID to 3500–6000 Å since the blue end of the spectrum contains more information about the SN and evolves more consistently with time for SNe II. Fixing the explosion epoch to JD 2,458,291.91 (from the EPM), we compared the spectra at 12.10, 19.06, 22.99, and 27.29 days with the SNID templates, where the explosion epochs are given by the EPM. The top five matches were then averaged to compute the epoch of the spectra, and the error was given by the standard deviation. The epochs of the spectra derived from this method are 10.84 ± 1.87 , 17.82 ± 4.74 , 25.02 ± 4.65 , and 31.74 ± 6.79 days, respectively, consistent with the spectral epochs inferred from the EPM.

5. Photometric Evolution

The full multiband light curves of SN 2018cuf are shown in Figure 2. The V-band light curve shows an initial rise to reach a maximum brightness of $M_V = -16.73 \pm 0.32$ mag on JD 2,458,300.537, ~ 9 days after the date of explosion. A plateau of approximately constant brightness follows due to the hydrogen envelope recombination that extends up to roughly day 112. The other filters show similar trends with bluer bands peaking slightly earlier and redder bands later. Following the plateau phase, the light curves show an unusually slow drop and finally settles onto a linear decline phase.

After the maximum brightness, the SN II light curves exhibit a wide range of properties. In order to understand where SN 2018cuf lies in the family of SNe II, we measured several light-curve parameters and compared them with those of other SNe II. One of the most studied parameters is the rate of decline after maximum light, which is used to classify subtypes of SNe II into SNe IIP and SNe IIL (“L” for linear). Statistical analyses of SNe II also point out that there is a correlation between the decline rate and the maximum absolute magnitude (Li et al. 2011; Anderson et al. 2014; Galbany et al. 2016b; Valenti et al. 2016). Following Valenti et al. (2016) we measured the slope of the light curve per 50 days in the V band (S_{50V}) of SN 2018cuf. We found $S_{50V} = 0.21 \pm 0.05$ mag (50 days) $^{-1}$, which combined with M_V (see Figure 8) places SN 2018cuf nicely within the region of SNe IIP.

After ~ 100 days, the light curves of SNe II transition from being powered primarily by the recombination in the photosphere to being powered by the radioactive decay of $^{56}\text{Ni} \rightarrow ^{56}\text{Co} \rightarrow ^{56}\text{Fe}$. This period, known as the fall from the plateau, can be characterized as a Fermi–Dirac function

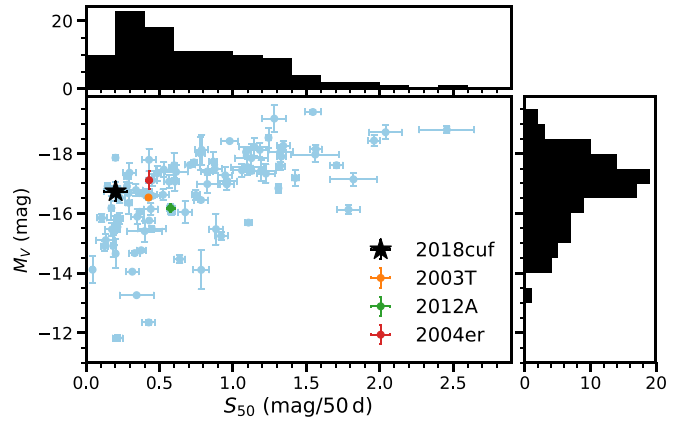


Figure 8. The M_V compared to S_{50V} for SN 2018cuf and a sample of SNe II. The SNe in this sample are from Anderson et al. (2014) and Valenti et al. (2016) and are available in Sndavis. In this plot, IIP-like SNe are usually located toward the left, and IIL-like SNe are located toward the right. SN 2018cuf, SN 2003T, SN 2004er, and SN 2012A are highlighted with different colors, and a detailed discussion of these four objects can be found in Section 5.

(Olivares et al. 2010; Valenti et al. 2016):

$$y(t) = \frac{-a0}{1 + e^{(t-t_{PT})/\omega0}} + (p0 \times (t - t_{PT})) + m0, \quad (3)$$

where t_{PT} refers to the length of the plateau, $\omega0$ indicates the slope of the light curve during the post-plateau phase (a large $\omega0$ implies a small slope), and $a0$ is the depth of the drop. We fit the V-band light curve using the package emcee (Foreman-Mackey et al. 2013), and the best-fitting values were found to be $t_{PT} = 112.24^{+0.71}_{-0.68}$ days, $\omega0 = 7.87^{+0.64}_{-0.59}$ days, and $a0 = 1.99^{+0.052}_{-0.049}$ mag. We found that SN 2018cuf has one of the highest $\omega0$ values in our sample of SNe II from the Sndavis database³³ (see Figure 9), indicating that the slope of the fall from the plateau is shallower than those of most SNe II. Another SN with a slow fall from the plateau is SN 2004er (Anderson et al. 2014; see Figure 10), but sparse data on the tail and a lack of multicolor observations make further comparisons difficult.

The effect of ^{56}Ni mixing on the SN light curve, particularly in relation to the fall from the plateau, has been studied by many authors (e.g., Kasen & Woosley 2009; Bersten et al. 2011; Goldberg et al. 2019). It is possible that the slow fall from the plateau is related to a low mixing of the ^{56}Ni distribution in the ejecta at the moment of explosion. For instance, Goldberg et al. (2019) produced several model light curves with different ^{56}Ni distributions (see their Figure 10), showing that insufficient mixing of ^{56}Ni results in a shallow slope in the post-plateau phase. Alternatively, increasing the total mass of ^{56}Ni can also lead to a shallower fall from the plateau (e.g., see Figure 2 in Kasen & Woosley 2009 and Figure 13 in Goldberg et al. 2019).

Which of these two effects, ^{56}Ni mixing or total ^{56}Ni mass, is more important to explain the shallow slope of SN 2018cuf is unclear. To try to disentangle these effects, we identified two other Type IIP SNe, SN 2012A and SN 2003T, in the literature that have either a similar progenitor (the progenitor of SN 2018cuf is discussed in Section 7) or light-curve parameters similar to those of SN 2018cuf. The V-band light curve of

³³ <http://dark.physics.ucdavis.edu/sndavis/transient>

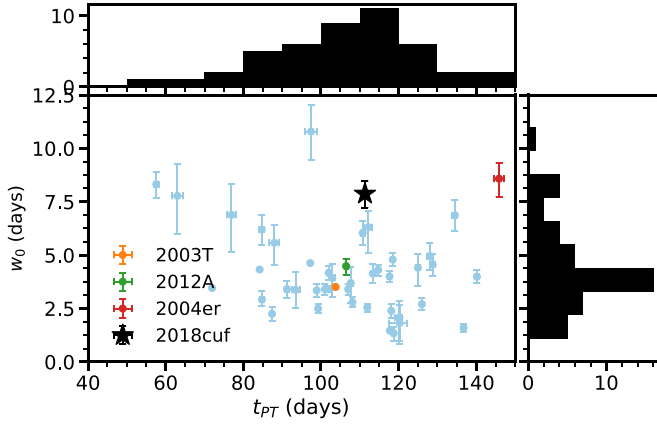


Figure 9. Comparison of t_{PT} and w_0 for V band as described in the text. A large w_0 implies a shallow post-plateau slope. SN 2018cuf, SN 2003T, SN 2004er, and SN 2012A are highlighted with different colors.

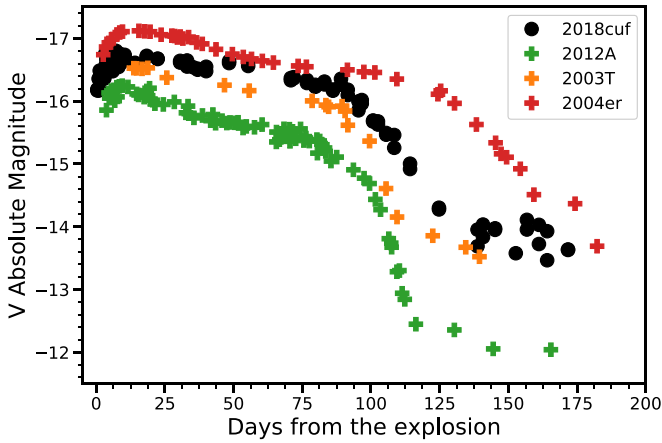


Figure 10. V-band light curves of SN 2018cuf, SN 2003T, SN 2012A, and SN 2004er compared in terms of absolute magnitude. As can be seen in Figure 8, SN 2012A and SN 2003T peak at roughly the same magnitude as SN 2018cuf but have a slightly steeper post-plateau slope. SN 2004er has a shallow post-plateau slope, similar to SN 2018cuf, but with a much brighter absolute magnitude and a much longer plateau phase.

SN 2018cuf is compared with those of the other SNe in Figure 10. All three objects are spectroscopically similar with roughly the same maximum absolute magnitude (see Figure 8) and plateau length. The progenitor of SN 2012A has been well studied (Tomasella et al. 2013; Utrobin & Chugai 2015; Morozova et al. 2018), and it has a progenitor mass, radius, and explosion energy similar to those of the progenitor of SN 2018cuf but a lower nickel mass. Additionally, SN 2012A has a maximum magnitude similar to that of SN 2018cuf but a steeper fall from the plateau (see Figure 10). By comparing SN 2018cuf with SN 2012A, we may then conclude that the shallow slope of the fall from the plateau of SN 2018cuf is due to the larger nickel mass produced by SN 2018cuf. On the other hand, a different conclusion is supported by comparing SN 2018cuf with SN 2003T. The nickel mass of SN 2003T is very similar to that of SN 2018cuf according to its tail magnitude, while the fall from the plateau of SN 2003T is much faster than that of SN 2018cuf, suggesting that a low degree of nickel mixing in SN 2018cuf could also contribute to the shallow fall from the plateau. In addition, the ^{56}Ni mass of SN 2018cuf is measured to be 0.04 (0.01) M_{\odot} (see Section 7). This is consistent with the amount of

nickel typically produced in SNe II (Anderson et al. 2014; Müller et al. 2017; Anderson 2019). Since the ^{56}Ni mass of SN 2018cuf is typical for the Type II family, it is more likely that the shallow slope is due to mixing; however, both scenarios are possible and we are unable to conclusively disentangle the effects.

6. Spectroscopic Evolution

6.1. Optical Spectra

The optical spectroscopic evolution of SN 2018cuf is shown in Figure 4. The early spectrum shows a blue continuum with a broad $H\alpha$ line clearly detected. Over time, the spectra become redder and develop hydrogen Balmer lines with P Cygni features. The $[\text{Fe II}] \lambda\lambda 4924, 5018, \text{ and } 5169$ lines, good tracers for the photospheric velocity, can be seen after day 17. Other typical features such as $[\text{Ca II}] \lambda\lambda 3934, 3968$, the Ca II infrared triplet $\lambda\lambda 8498, 8542, 8662$, and $\text{NaID } \lambda\lambda 5890, 5896$ also appear in emission as the SN evolves. During the nebular phase, strong $[\text{Ca II}] \lambda\lambda 7291, 7324$ emission lines emerge along with $[\text{Fe II}] \lambda 7155$, $[\text{He I}] \lambda 6678$, and $[\text{O I}] \lambda\lambda 6300, 6364$.

Interestingly, from day 105 to day 174, a small notch appears on the $H\alpha$ profile with a velocity of $\sim 1000 \text{ km s}^{-1}$, and its origin is unclear. One possibility is that this feature is from dust formation either in the ejecta or in circumstellar material (CSM) interaction. The signatures of dust formation have been detected in many Type II SNe. Type II SNe SN2010jl shows notches or double-peaked profiles at an earlier stage and later shows more dominant blue-wings (see Extended Data Figure 3 of Gall et al. 2014). Type II SNe SN1998S also shows a notch feature in its broad emission lines (Mauerhan & Smith 2012). However, for SN 2018cuf, this notch feature emerges starting at day 106, and the temperature of the ejecta may still be too hot for dust formation. On the other hand, the feature is not detected in the spectra after day 293, which is hard to reconcile with dust formation. By comparing $H\alpha$ with other hydrogen line profiles, we do not find any evidence of red-side attenuation for lines that occur at bluer wavelengths, as is expected for dust creation. For these reasons, we cannot unambiguously attribute this feature to dust formation and equally rule out the possibility of dust formation.

The evolution of $H\alpha$ and $H\beta$ lines during the photospheric phase is shown in Figure 11. Starting at day 22, an extra absorption line can be seen on the blue side of the $H\alpha$ and $H\beta$ P Cygni absorption lines, becoming more obvious by day 34. These lines have been studied in many SNe II and have been most often associated with $[\text{Si II}] \lambda 6355$ when seen at early phases (< 30 days) and with HV hydrogen when seen at a later phase (50–100 days; e.g., Chugai et al. 2007; SN2005cs, Pastorello et al. 2006; SN2009bw, Inserra et al. 2012; SN2013ej, Valenti et al. 2014). This ambiguous absorption feature is often referred to as the “Cachito” feature (Gutiérrez et al. 2017). In the case of SN 2018cuf, because this feature appears at roughly 30 days, it is likely associated with HV hydrogen, an interpretation that is confirmed by the additional presence of the HV feature in $H\beta$ at similar velocities.

6.2. Near-infrared Spectra

The NIR spectra from day 4 to day 94 are plotted in Figure 5 and show an evolution typical of SN II. The first spectrum at day 4 is nearly featureless with weak Paschen lines, but by day

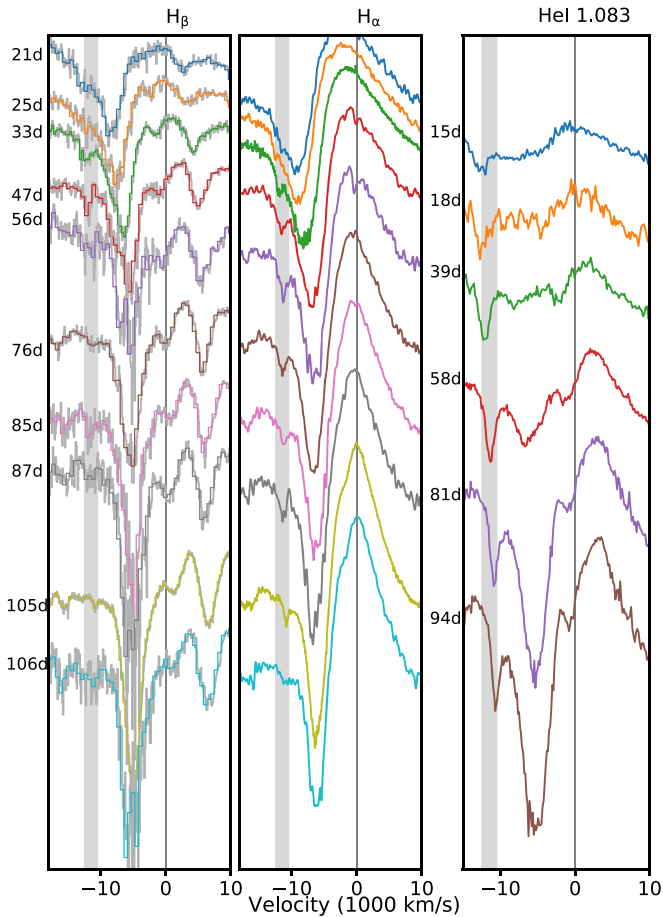


Figure 11. The evolution of Cachito features in $H\alpha$, $H\beta$, and $\text{He I } \lambda 1.083 \mu\text{m}$ during the photospheric phase. In the left panel, the spectra from FLOYDS and SALT are binned to 9 \AA pixel^{-1} and 5 \AA pixel^{-1} , respectively, and the gray background lines are the original spectra. The shaded area marks $-12,500 \text{ km s}^{-1}$ to $-10,500 \text{ km s}^{-1}$. The Cachito features in all three lines show consistent velocities, supporting their presence as HV features.

15 these features have strengthened and $[\text{He I}] \lambda 10830$ has also appeared. Both $\text{Pa } \alpha$ and $\text{Br } \gamma$ lines can be seen in our spectra after day 58.

In general, the line evolution in NIR spectra is consistent across SNe II. However, Davis et al. (2019) pointed out that SNe II can be classified as spectroscopically strong or weak based on the pseudo-equivalent width (pEW) of the $[\text{He I}] \lambda 10830$ absorption line and the features seen in the spectra. They found that SNe with weak He I (pEW $< 50 \text{ \AA}$) are slow-declining SNe IIP and that SNe with strong He I (pEW $> 50 \text{ \AA}$) correspond to the faster-declining Type IIL SNe class. Interestingly, SN 2018cuf seems to be an exception to this rule. The pEWs of He I absorption for days 39, 58, 81, and 94 are 4.9 \AA , 25.2 \AA , 82.5 \AA , and 105 \AA , respectively, which makes it hard to classify it as either a strong or weak SN based on the pEW alone. In addition to smaller pEWs, weak SNe usually show the $\text{P}\gamma/\text{Sr II}$ absorption feature at earlier epochs (~ 20 days after explosion) and are accompanied by an HV He I feature. For SN 2018cuf, the $\text{P}\gamma/\text{Sr II}$ absorption feature shows up at day 18, consistent with a weak SN. Additionally, there is clearly an extra absorption feature on the blue side of He I (see the right panel of Figure 5 or Figure 11). Other than HV He I, this feature could also be explained as $[\text{C I}] \lambda 10693$. However, the lack of other C I lines in the NIR

spectra makes it unlikely that this feature originates from $[\text{C I}] \lambda 10693$. We also note that the velocity of HV He I matches the velocity of HV $H\alpha$ and HV $H\beta$ in optical spectra, which further strengthens our conclusion that this feature can be interpreted as HV He I. Although the pEW of SN 2018cuf is greater than the 50 \AA limit used in Davis et al. (2019), the presence of $\text{P}\gamma/\text{Sr II}$ at an early phase and of HV He I suggests that our object still falls into the weak SN II category. This implies that the 50 \AA limit from Davis et al. (2019) is probably too low.

Chugai et al. (2007) proposed that HV absorption features, like those seen in SN 2018cuf, come from the interaction between the circumstellar wind and the SN ejecta. They argued that there are two physical origins of HV absorption: enhanced excitation of the outer layers of unshocked ejecta, which contributes to the shallow HV absorption in the blue side of $H\alpha$ and $[\text{He I}] \lambda 10830$, and the cold dense shell (CDS), which is responsible for the HV notch in the blue wing of $H\alpha$ and $H\beta$. For the former case, the $H\beta$ HV is not expected to be seen due to the low optical depth in $H\beta$ line-forming regions, whereas in the latter case an HV Cachito can form in both $H\alpha$ and $H\beta$. For SN 2018cuf, the presence of Cachito features in $H\alpha$, $H\beta$, and $[\text{He I}] \lambda 10830$ supports the CDS interpretation but does not completely rule out the first scenario.

$\text{Pa}\beta$ and $\text{Pa}\gamma$ were also investigated to look for HV features. However, the existence of other strong lines around $\text{Pa}\gamma$ makes it difficult to identify an HV feature if present, and there is no HV feature in the blue side of $\text{Pa}\beta$. Chevalier & Fransson (1994) suggested that the temperature of the CDS should be low enough that this region is dominated by low-ionization lines, which causes $\text{Pa}\beta$ absorption to form in a low optical depth region and may explain the absence of HV features in $\text{Pa}\beta$.

7. Progenitor Properties

7.1. Nickel Mass

The nebular phase of SNe II is driven by radioactive decay $^{56}\text{Ni} \rightarrow ^{56}\text{Co} \rightarrow ^{56}\text{Fe}$. If the γ -rays produced by this process are completely trapped by the ejecta, the bolometric luminosity at late times can be used to estimate the amount of ^{56}Ni . Since our photometry after ~ 100 days does not cover the full spectral energy distribution (SED), we used two different methods to derive the ^{56}Ni mass. The first method is to calculate the pseudo-bolometric luminosity of SN 2018cuf and compare it with the pseudo-bolometric light curve of SN 1987A. Assuming SN 2018cuf and SN 1987A have the same normalized SED, the nickel mass is given by Spiro et al. (2014):

$$M_{\text{Ni}} = 0.075 \times \frac{L_{\text{SN}}}{L_{87A}} M_{\odot} \quad (4)$$

where L_{SN} and L_{87A} are the pseudobolometric luminosity of SN 2018cuf and SN 1987A, respectively. For the pseudo-bolometric luminosity, we followed the method described by Valenti et al. (2008). The observed magnitudes were converted to flux at each band and integrated by using Simpson's rule, which uses a quadratic polynomial to approximate the integral. The photometric data from day 135 to day 170 were used to calculate the pseudo-bolometric luminosities of SN 2018cuf and SN 1987A by using passbands $\{\text{BVgri}\}$ and $\{\text{BVRI}\}$, respectively, resulting in a ^{56}Ni mass of $0.037^{+0.003}_{-0.002} M_{\odot}$.

An alternative approach to estimate the nickel mass is to compute a full-band bolometric light curve by performing a

blackbody fit to all available filters at each photometric epoch and integrating the blackbody. The advantage of this method is that it does not require the assumption that SN 2018cuf and SN 1987A have the same normalized SED, although the approximation to a blackbody may not be completely valid due to the line blanketing in the UV bands. The ^{56}Ni mass derived from this approach is $0.042^{+0.045}_{-0.008} M_{\odot}$. Given the limitations of each method, we chose to use the pseudobolometric luminosity method to estimate the ^{56}Ni mass but took the difference between the results from the two methods as an indicator of the uncertainty of the measurement. The final nickel mass was conservatively estimated to be $M_{\text{Ni}} = 0.04$ (0.01) M_{\odot} . By comparing the pseudobolometric light curve of SN 2018cuf with that of SN 1987A, we found that the decline rate of SN 2018cuf in the radioactive tail is either consistent with or slightly faster than ^{56}Co decay. It is hard to be sure which one is the case here due to the lack of data in the radioactive tail. If the decline rate of SN 2018cuf is slightly faster than ^{56}Co decay, the ^{56}Ni mass we derived here could be treated as a lower limit.

7.2. Progenitor Mass

Progenitor mass is a fundamental parameter of an SN, and it can be constrained by using multiple techniques. In this section, we derive the progenitor mass of SN 2018cuf from nebular spectra and hydrodynamic light-curve modeling.

7.2.1. From Nebular Spectroscopy

During the nebular phase, spectra can provide useful information about the inner structure of an SN. At this stage, the ejecta has become optically thin, revealing the core nucleosynthesis products. The strength of the [O I] $\lambda\lambda 6300, 6364$ doublet in the nebular spectra has been found to be a good indicator of progenitor mass (Jerkstrand et al. 2014). By comparing the intensities of [O I] $\lambda\lambda 6300, 6364$ with theoretical models during this phase, the progenitor mass can be well constrained. Jerkstrand et al. (2014) modeled the nebular spectra for 12, 15, 19, and 25 M_{\odot} progenitors at different phases. They started with the SN ejecta evolved and exploded with KEPLER (Woosley & Heger 2007) and used the spectral synthesis code described in Jerkstrand et al. (2011) to generate the model spectra.

Although we have six nebular spectra for SN 2018cuf taken from day 174 to day 483, four of them are contaminated by the host galaxy. Therefore, we only compare the nebular spectra of SN 2018cuf at day 174 and day 336 with the models computed by Jerkstrand et al. (2014) in Figure 12. We scaled the nebular spectra taken at day 174 and day 336 to the r -band photometry, and the models were scaled to the observed spectrum so that they had the same integrated flux. We found that the strength of O I in our spectrum is between the 12 M_{\odot} and the 15 M_{\odot} models, which implies the progenitor mass of SN 2018cuf is likely in this range.

Synthetic nebular spectra can also be used to give an independent estimate of the nickel mass (Jerkstrand et al. 2018; Bostroem et al. 2019). By using the scale factors we used to scale the model spectra, the nickel mass can be derived using the following relation from Bostroem et al. (2019):

$$\frac{F_{\text{obs}}}{F_{\text{mod}}} = \frac{d_{\text{mod}}^2}{d_{\text{obs}}^2} \frac{M_{^{56}\text{Ni}_{\text{obs}}}}{M_{^{56}\text{Ni}_{\text{mod}}}} \exp\left(\frac{t_{\text{mod}} - t_{\text{obs}}}{111.4}\right) \quad (5)$$

where F_{obs} is the total observed flux and F_{mod} is the total flux from the model spectrum. d_{obs} is the distance of the SN and

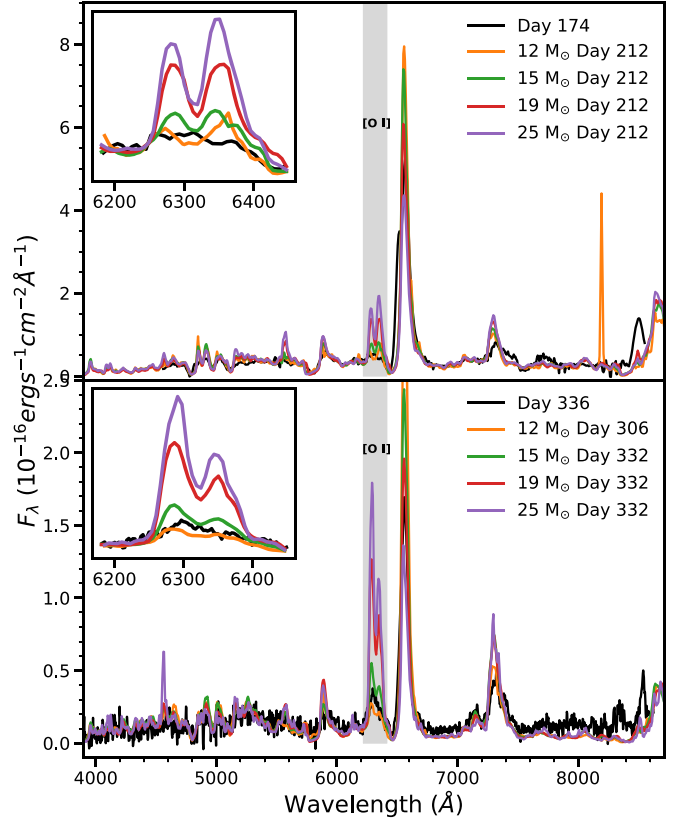


Figure 12. Comparison of the nebular spectra of SN 2018cuf from day 174 and day 336 with four models at similar epochs. The insets show the [O I] doublet, which is a good indicator of progenitor mass. From this line, we estimated the progenitor mass to be between 12 and 15 M_{\odot} as discussed in the text.

$d_{\text{mod}} = 5.5$ Mpc is the distance used to compute the model; $M_{^{56}\text{Ni}}$ indicates the nickel mass for the SN ($M_{^{56}\text{Ni}_{\text{obs}}}$) and the model ($M_{^{56}\text{Ni}_{\text{mod}}} = 0.062 M_{\odot}$), and t_{obs} and t_{mod} are the phase of the spectra for the observation and model, respectively. We then derived nickel masses of $0.040^{+0.004}_{-0.003} M_{\odot}$ and $0.060^{+0.006}_{-0.016} M_{\odot}$ for day 174 and day 336, respectively. These values are consistent with what we got in the previous subsection, where we measured the nickel mass from the radioactive decay tail photometry when the SN just falls from the plateau (days 135–170).

7.2.2. From Hydrodynamic Modeling

An alternative way of constraining the mass of the progenitor is to compare the light curves to hydrodynamic models (e.g., Utrobin & Chugai 2015, 2017; Morozova et al. 2017, 2018; Paxton et al. 2018; Goldberg et al. 2019; Martinez & Bersten 2019). We used the Supernova Explosion Code (SNEC; Morozova et al. 2015), an open-source hydrodynamic code for core-collapse SNe, to constrain the progenitor parameters of SN 2018cuf. SNEC assumes diffusive radiation transport and local thermodynamic equilibrium, which are valid assumptions from shock breakout through the end of the plateau. However, as the SN becomes nebular, this assumption breaks down. For this reason, we compared our light curve only out to $t_{\text{PT}} = 112.24$ days with the SNEC models. Our inputs of evolved progenitor stars for SNEC are the nonrotating solar metallicity RSG models generated from the KEPLER code and described in Sukhbold et al. (2016). A steady-state wind with a

density profile

$$\rho(r) = \frac{\dot{M}}{4\pi r^2 \nu_{\text{wind}}} = \frac{K}{r^2} \quad (6)$$

is also added above these models to explore the effect of CSM on light curves, where \dot{M} is the wind mass-loss rate and ν_{wind} is the wind velocity. We will use the parameter K to describe the constant wind density, which extends up to radius R_{ext} . For each explosion, SNEC takes a variety of progenitor and explosion parameters as input and then generates a bolometric light curve and, assuming blackbody radiation, the optical light curves. We followed the approach of Morozova et al. (2017), exploring variations in progenitor mass (M), nickel mass, explosion energy (E), K , and R_{ext} and fixing the nickel mass to $M_{\text{Ni}} = 0.04 M_{\odot}$, which we obtained from the tail photometry. We note that the degree of ^{56}Ni mixing can also be a free parameter in SNEC models. However, the SNEC model cannot reproduce the light curves well during the fall from the plateau since the radiation diffusion approach used in SNEC is no longer valid during and after this period, so we were not able to use SNEC to explore the effect of ^{56}Ni mixing on the postplateau light curves. Morozova et al. (2015) also found that the light curves generated by SNEC are not sensitive to the degree of ^{56}Ni mixing, so we fixed the initial ^{56}Ni mixing and mixed ^{56}Ni up to $5 M_{\odot}$ in the mass coordinates.

Morozova et al. (2018) pointed out that only the early phase of the light curve is dominated by CSM, so it is possible to adopt a two-step approach to fit the light curves. In the first step, we evaluated the fit for the part of the light curve that is mostly dominated by the hydrogen-rich envelope and varied only M and E . The fitting range was chosen to be between the end of $s1$ (37.19 days from explosion for SN 2018cuf) and t_{PT} , where $s1$ is the initial steeper slope of the light curve. This allowed us to determine the best-fit progenitor mass and explosion energy. In the next step, we fixed the progenitor mass and explosion energy found in step one, and we explored the influence of CSM, varying K and R_{ext} and fitting the whole light curve through t_{PT} . This substantially reduced the number of models needed to explore the parameter space, allowing us to search over a finer grid in each parameter.

At each stage, the best-fit model was determined by interpolating the models to the observed epochs in g , r , i filters and minimizing χ^2 over these filters. For the first stage, the range of parameters considered is $10 M_{\odot} < M < 30 M_{\odot}$ and $0.1 < E < 1.2$ (in units of 10^{51} erg). We obtained a best fit of $M = 14.5 M_{\odot}$, which corresponds to an $827 R_{\odot}$ progenitor star from Table 2 of Sukhbold et al. (2016), and $E = 5.71 \times 10^{50}$ erg as shown in the upper panel of Figure 13. In the next step, the CSM parameter range was set to $2 < K < 20$ (in units of $10^{17} \text{ g cm}^{-1}$) and $827 R_{\odot} < R_{\text{ext}} < 3000 R_{\odot}$, and the fitting range also included the early part of the light curve, i.e., we fit the light curves from the explosion to t_{PT} . The result is presented in the middle panel of Figure 13, and the best-fitting model is $K = 3.1 \times 10^{17} \text{ g cm}^{-1}$ and $R_{\text{ext}} = 1369 R_{\odot}$. In the bottom panel of Figure 13, we show the light curves of the best-fitting models with and without dense CSM. The progenitor mass ($14.5 M_{\odot}$) we got from the SNEC model is in good agreement with what we got from the synthetic nebular spectrum analysis ($12\text{--}15 M_{\odot}$), and this is a moderate mass for an SN II. It should be noted that we did not fit the model

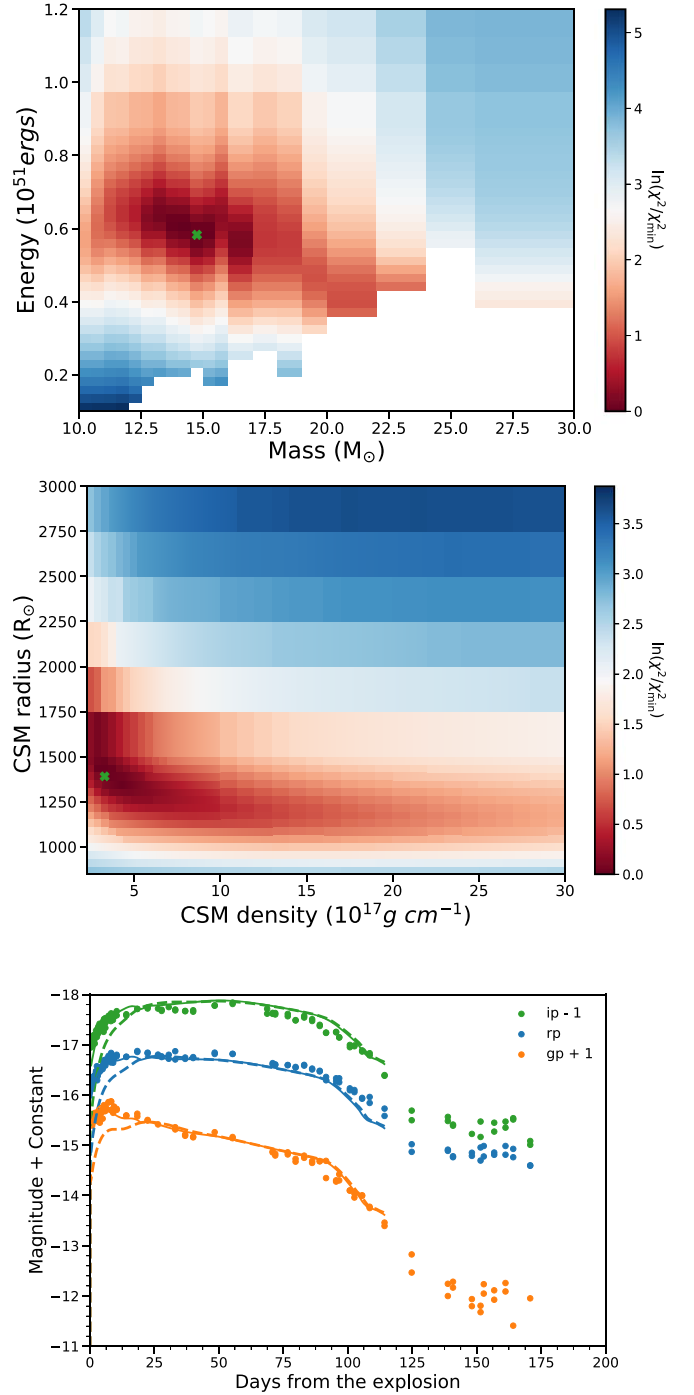


Figure 13. Top and middle: The color indicates the χ^2 value, and the green cross represents the best-fitting SNEC model. Bottom: The dots are the observational data, while the different colors represent the different bands. The solid lines and dashed lines are the best-fitting SNEC model with and without CSM, respectively.

photospheric velocity with the ejecta velocity derived from the [Fe II] $\lambda 5169$ line. Both Goldberg et al. (2019) and Goldberg & Bildsten (2020) pointed out that fitting the ejecta velocities inferred from the [Fe II] $\lambda 5169$ line can barely break the degeneracy between the explosion properties, so we chose not to fit the ejecta velocity in our SNEC modeling.

Previous work (Morozova et al. 2017, 2018; Bostroem et al. 2019) has found that there is a strong degeneracy between the

density profile and the external radius of CSM and the total mass of CSM derived from the fits is more robust. If we adopt a progenitor radius of $827 R_{\odot}$ as the inner CSM radius, the total CSM mass of our best-fit model will be $0.07 M_{\odot}$ by integrating Equation (6) over r . If we interpret this wind as that of a typical RSG, adopting a wind speed of 10 km s^{-1} , the mass-loss rate would be $0.06 M_{\odot} \text{ yr}^{-1}$ within a timescale of 14 months, much higher than those of the steady winds observed in RSGs (Smith 2014). The possible explanation is that such dense CSM may originate from pre-SN outbursts due to the late-stage nuclear burning in the stellar interior (Quataert & Shiode 2012; Smith & Arnett 2014; Fuller 2017; Ouchi & Maeda 2019; Morozova et al. 2020). Due to the presence of dense CSM around the SN, flash signatures may also be seen in the early spectrum (Yaron et al. 2017; Nakaoka et al. 2018; Rui et al. 2019). However, such a signature is not found for SN 2018cuf, which may imply that the dense CSM is very close to the progenitor, consistent with the small CSM radial extent derived from the SNEC model.

7.3. Shock Cooling Model

After the shock breakout, the SN emission is dominated by shock cooling and carries useful information about the radius and pre-explosion evolution of the progenitor star system. Sapir & Waxman (2017) updated the model presented by Rabinak & Waxman (2011) and found that the photospheric temperature and bolometric luminosity during the early phase for an SN with an RSG progenitor (convective envelope with $n = 3/2$) can be written as

$$T(t) = T_1 * t_d^{-0.45} \quad (7)$$

$$L(t) = L_1 \exp \left[- \left(\frac{1.67 * t_d}{t_{tr}} \right)^{0.8} \right] * t_d^{-0.17}, \quad (8)$$

where T_1 and L_1 are the temperature and the luminosity ~ 1 day after the explosion, respectively, t_d is the time from explosion, and t_{tr} is the time when the envelope is starting to become transparent. We applied this model to SN 2018cuf, which was discovered well before t_{tr} , using the code developed by Hosseinzadeh et al. (2018) and Hosseinzadeh (2020). This Markov Chain Monte Carlo (MCMC) routine was adopted to give the posterior probability distributions of T_1 , L_1 , t_{tr} , and t_0 simultaneously, where t_0 is the explosion epoch. This analytical model is only valid for $T < 0.7 \text{ eV}$, and we have checked that the final fitting results satisfy this condition. The MCMC converges to an explosion epoch of $\text{MJD } 58,287.8 \pm 0.2$ (or $\text{JD } 2,458,288.3 \pm 0.2$), which is about 3 days earlier than our last nondetection ($\text{JD } 2,458,291.74$). An explosion epoch earlier than our first nondetection is possible as the SN may be below our detection limits shortly after explosion. However, in order to fit the U - and V -band light curves, we required $t_{tr} = 10,000$ days, which is unphysically late. For this reason we did not attempt to derive progenitor or explosion parameters using this method. The inability of this method to fit the blue part of the light curve has been noted by several authors (Arcavi et al. 2017; Hosseinzadeh et al. 2018). One possible reason for the fitting failure could be that there is a CSM–ejecta interaction around the progenitor, which is supported by the light-curve modeling as we discussed in the last subsection. In

addition, the effect of UV-band line blanketing is underestimated in the model spectrum, so that assuming blackbody radiation cannot well reproduce the light curves in UV bands.

8. Conclusions

In this paper, we have presented spectroscopic and photometric observations of SN 2018cuf in the galaxy IC 5092. The object was discovered by the DLT40 survey within ~ 1 day of explosion, and the well-sampled light curves and spectra from GSP were used to constrain the progenitor properties. In general, SN 2018cuf is consistent with other SNe II, while it has a relatively slow fall from the plateau, which could be a result of insufficient mixing of ^{56}Ni or a high ^{56}Ni mass. During the plateau phase, we identified HV features in $\text{H}\alpha$, $\text{H}\beta$, and $\text{He I } \lambda 10830$, suggesting interaction between ejecta and CSM.

We used the EPM to derive a distance of $41.8 \pm 5.8 \text{ Mpc}$ to SN 2018cuf and an explosion epoch of $\text{JD } 2,458,292.81 \pm 3.08$, which is confirmed by SNID and consistent with the last nondetection from DLT40. From the pseudo-bolometric luminosity of the radioactive decay tail, the nickel mass is found to be $0.04 (0.01) M_{\odot}$, which is further confirmed by the nickel mass derived from nebular spectra. SNEC modeling was used to determine the progenitor parameters, finding a progenitor mass of $14.5 M_{\odot}$ with an explosion energy of $E \approx 5.71 \times 10^{50} \text{ erg}$ and a CSM mass of $M_{\text{CSM}} \approx 0.07 M_{\odot}$. The progenitor mass from SNEC is in good agreement with what we got from nebular spectral modeling ($12\text{--}15 M_{\odot}$). The dense CSM inferred from SNEC modeling may imply that the progenitor experienced some outbursts due to the late-stage nuclear burning before explosion. We also tried to apply the shock cooling model to the early light curve but found it yields unphysical results. From the SNEC model, we infer significant CSM around SN 2018cuf, which could be a main reason for the fitting failure, since the shock cooling model is no longer valid in the presence of dense CSM. In addition, the underestimation of the effect of UV-band line blanketing for the model spectra may have contributed to the failure of model fitting.

We found that, at least for this single object, hydrodynamical modeling and nebular spectral modeling give consistent progenitor mass. In the future, with more and more young SNe detected, we will be able to investigate the systematic bias for these techniques and finally have the ability to better understand the progenitors of SNe IIP.

We would like to thank Daniel Kasen and Nir Sapir for beneficial discussions. Research by Y.D., S.V., and K.A.B. is supported by National Science Foundation (NSF) grant AST-1813176. Research by D.J.S. is supported by NSF grants AST-1821967, 1821987, 1813708, 1813466, and 1908972 and by the Heising-Simons Foundation under grant #2020-1864. This work makes use of observations from the Las Cumbres Observatory network. D.A.H., J.B., and D.H. are supported by NSF grant AST-1911225 and NASA Swift grant 80NSSC19k1639. L.G. was funded by the European Union’s Horizon 2020 research and innovation program under the Marie Skłodowska-Curie grant agreement No. 839090. This work has been partially supported by the Spanish grant PGC2018-095317-B-C21 within the European Funds for Regional Development. The SALT observations presented here were made through Rutgers University programs

2018-1-MLT-006 and 2019-1-MLT-004 (principal investigator: Jha); supernova research at Rutgers is supported by NSF award AST-1615455. The GMOS observation, GS-2018A-Q-116, was conducted via the time exchange program between Gemini and the Subaru Telescope. E.Y.H. and S.D. acknowledge the support provided by the NSF under grant No. AST-1613472. I.A. is a CIFAR Azrieli Global Scholar in the Gravity and the Extreme Universe Program and acknowledges support from that program, from the European Research Council under the European Union’s Horizon 2020 research and innovation program (grant agreement No. 852097), from the Israel Science Foundation (grant Nos. 2108/18 and 2752/19), from the United States–Israel Binational Science Foundation, and from the Israeli Council for Higher Education’s Alon Fellowship. H.K. was funded by Academy of Finland projects 324504 and 328898. Based on observations collected at the European Southern Observatory under ESO program 0102.D-0356. X.W. is supported by the National Natural Science Foundation of China (NSFC grants 11633002 and 11761141001) and the National Program on Key Research and Development Project (grant No. 2016YFA0400803). L.W. is sponsored (in part) by the Chinese Academy of Sciences (CAS),

through a grant to the CAS South America Center for Astronomy in Santiago, Chile.

This research has made use of the NASA/IPAC Extragalactic Database, which is operated by the Jet Propulsion Laboratory, California Institute of Technology, under contract with the National Aeronautics and Space Administration.

Facilities: CTIO:PROMPT, Las Cumbres Observatory (FLOYDS, Sinistro), Magellan:Baade (FIRE), Magellan:Clay (MIKE), Gemini:South (FLAMINGOS-2), SAAO:SALT (RSS), Swift (UVOT), VLT:Yepun (MUSE), VLT (FORSS2), Gemini: South (GMOS).

Software: Astropy (Astropy Collaboration et al. 2013, 2018), lcoctsnpipe (Valenti et al. 2016), SNID (Blondin & Tonry 2007), SciPy (<https://www.scipy.org>), NumPy (<https://numpy.org>), PYRAF, HOTPANTS (Becker 2015), Matplotlib (Hunter 2007), Pandas (McKinney 2010).

Appendix

Table A1 lists a sample of photometric observations of SN 2018cuf. Table A2 shows a log of the spectroscopic observations of SN 2018cuf.

Table A1
SN 2018cuf Optical Photometry

Date	Julian Date (days)	Phase (days)	Magnitude	Magnitude Error	Filter	Source
2018-06-19	2,458,288.78	−4.03	>19.70	0.0	Open	Prompt5
2018-06-21	2,458,290.83	−1.98	>19.68	0.0	Open	Prompt5
2018-06-22	2,458,291.74	−1.07	>19.38	0.0	Open	Prompt5
2018-06-23	2,458,292.86	0.05	17.44	0.02	Open	Prompt5
2018-06-23	2,458,293.20	0.39	16.63	0.02	<i>U</i>	COJ 1 m
2018-06-23	2,458,293.21	0.40	16.68	0.02	<i>U</i>	COJ 1 m
2018-06-23	2,458,293.21	0.40	17.34	0.02	<i>B</i>	COJ 1 m
2018-06-23	2,458,293.21	0.41	17.34	0.02	<i>B</i>	COJ 1 m
2018-06-23	2,458,293.22	0.41	17.35	0.01	<i>V</i>	COJ 1 m
2018-06-23	2,458,293.22	0.41	17.34	0.01	<i>V</i>	COJ 1 m
2018-06-23	2,458,293.22	0.41	17.21	0.01	<i>g</i>	COJ 1 m

(This table is available in its entirety in machine-readable form.)





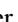


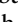
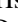



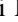










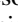


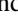
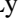


Table A2
SN 2018cuf Spectra

UT Date	Julian Date (days)	Phase (days)	Telescope	Instrument	Resolution ($\lambda/\Delta\lambda$)	Wavelength Range (\AA)
2018-06-24	2,458,293.73	0.92	Gemini	GMOS	1688	3916–7069
2018-06-24	2,458,294.50	1.69	SALT	RSS	600–2000	3533–7449
2018-06-25	2,458,294.50	1.69	SALT	RSS	600–2000	3497–7431
2018-06-27	2,458,296.50	3.69	Gemini	F2	900	9853–18081
2018-06-28	2,458,298.49	5.68	SALT	RSS	600–2000	3495–9396
2018-07-01	2,458,301.05	8.24	FTN	FLOYDS	400–700	4796–8996
2018-07-03	2,458,303.11	10.30	FTN	FLOYDS	400–700	3498–9999
2018-07-04	2,458,303.56	10.75	SALT	RSS	600–2000	3494–9393
2018-07-06	2,458,305.58	12.77	SALT	RSS	600–2000	3495–9396
2018-07-08	2,458,307.50	14.69	Gemini	F2	900	9851–18082
2018-07-10	2,458,310.07	17.26	FTN	FLOYDS	400–700	3498–9998
2018-07-11	2,458,310.50	17.69	Gemini	F2	900	9851–18081
2018-07-12	2,458,311.50	18.69	Magellan	MIKE	40000	4832–9415
2018-07-14	2,458,314.00	21.19	FTN	FLOYDS	400–700	3497–9998
2018-07-18	2,458,318.29	25.48	FTN	FLOYDS	400–700	3497–9999
2018-07-26	2,458,326.38	33.57	SALT	RSS	600–2000	3497–9398
2018-07-31	2,458,331.16	38.35	FTN	FLOYDS	400–700	4796–9996
2018-08-01	2,458,331.50	38.69	Gemini	F2	900	9847–18080
2018-08-09	2,458,339.96	47.15	FTN	FLOYDS	400–700	3498–9997
2018-08-18	2,458,348.92	56.11	FTN	FLOYDS	400–700	3497–9997

Table A2
(Continued)

UT Date	Julian Date (days)	Phase (days)	Telescope	Instrument	Resolution ($\lambda/\Delta\lambda$)	Wavelength Range (Å)
2018-08-20	2,458,350.50	57.69	Magellan	FIRE	300–500	7700–25269
2018-09-07	2,458,368.95	76.14	FTN	FLOYDS	400–700	3497–9997
2018-09-12	2,458,373.50	80.69	Magellan	FIRE	300–500	7755–25277
2018-09-16	2,458,377.92	85.11	FTN	FLOYDS	400–700	3498–9998
2018-09-18	2,458,379.96	87.15	FTN	FLOYDS	400–700	3497–9997
2018-09-25	2,458,386.50	93.69	Magellan	FIRE	300–500	7762–25297
2018-10-06	2,458,398.27	105.46	SALT	RSS	600–2000	3496–9395
2018-10-07	2,458,398.96	106.15	FTN	FLOYDS	400–700	3498–9998
2018-10-25	2,458,417.34	124.53	SALT	RSS	600–2000	3495–9394
2018-12-14	2,458,466.53	173.72	VLT	FORS	500	4608–8645
2019-04-12	2,458,585.50	292.69	VLT	MUSE	1700–3500	4750–9351
2019-05-25	2,458,628.65	335.84	SALT	RSS	600–2000	3898–8719
2019-05-26	2,458,629.53	336.72	SALT	RSS	600–2000	5899–8870
2019-06-23	2,458,658.46	365.65	SALT	RSS	600–2000	5900–9002
2019-10-19	2,458,776.29	483.48	SALT	RSS	600–2000	3921–7798

ORCID iDs

Yize Dong (董一泽)  <https://orcid.org/0000-0002-7937-6371>
 S. Valenti  <https://orcid.org/0000-0001-8818-0795>
 K. A. Bostroem  <https://orcid.org/0000-0002-4924-444X>
 D. J. Sand  <https://orcid.org/0000-0003-4102-380X>
 Jennifer E. Andrews  <https://orcid.org/0000-0003-0123-0062>
 L. Galbany  <https://orcid.org/0000-0002-1296-6887>
 Saurabh W. Jha  <https://orcid.org/0000-0001-8738-6011>
 Lindsey Kwok  <https://orcid.org/0000-0003-3108-1328>
 E. Y. Hsiao  <https://orcid.org/0000-0003-1039-2928>
 Scott Davis  <https://orcid.org/0000-0002-2806-5821>
 Peter J. Brown  <https://orcid.org/0000-0001-6272-5507>
 H. Kuncarayakti  <https://orcid.org/0000-0002-1132-1366>
 Keiichi Maeda  <https://orcid.org/0000-0003-2611-7269>
 Jeonghee Rho  <https://orcid.org/0000-0003-3643-839X>
 R. C. Amaro  <https://orcid.org/0000-0002-1546-9763>
 J. P. Anderson  <https://orcid.org/0000-0003-0227-3451>
 Iair Arcavi  <https://orcid.org/0000-0001-7090-4898>
 Raya Dastidar  <https://orcid.org/0000-0001-6191-7160>
 Daichi Hiramatsu  <https://orcid.org/0000-0002-1125-9187>
 Griffin Hosseinzadeh  <https://orcid.org/0000-0002-0832-2974>
 D. Andrew Howell  <https://orcid.org/0000-0003-4253-656X>
 J. Jencson  <https://orcid.org/0000-0001-5754-4007>
 Vladimir Kouprianov  <https://orcid.org/0000-0003-3642-5484>
 M. Lundquist  <https://orcid.org/0000-0001-9589-3793>
 J. D. Lyman  <https://orcid.org/0000-0002-3464-0642>
 Curtis McCully  <https://orcid.org/0000-0001-5807-7893>
 Kuntal Misra  <https://orcid.org/0000-0003-1637-267X>
 Daniel E. Reichart  <https://orcid.org/0000-0002-5060-3673>
 S. F. Sánchez  <https://orcid.org/0000-0001-6444-9307>
 Nathan Smith  <https://orcid.org/0000-0001-5510-2424>
 Lingzhi Wang  <https://orcid.org/0000-0002-1094-3817>
 S. Wyatt  <https://orcid.org/0000-0003-2732-4956>

References

Anderson, J. P. 2019, *A&A*, 628, A7
 Anderson, J. P., Dessart, L., Gutiérrez, C. P., et al. 2018, *NatAs*, 2, 574
 Anderson, J. P., González-Gaitán, S., Hamuy, M., et al. 2014, *ApJ*, 786, 67

Appenzeller, I., Fricke, K., Fürtig, W., et al. 1998, *Msngr*, 94, 1
 Arcavi, I., Hosseinzadeh, G., Brown, P. J., et al. 2017, *ApJL*, 837, L2
 Asplund, M., Grevesse, N., Sauval, A. J., & Scott, P. 2009, *ARA&A*, 47, 481
 Astropy Collaboration, Price-Whelan, A. M., Sipőcz, B. M., et al. 2018, *AJ*, 156, 123
 Astropy Collaboration, Robitaille, T. P., Tollerud, E. J., et al. 2013, *A&A*, 558, A33
 Baade, W. 1926, *AN*, 228, 359
 Bacon, R., Accardo, M., Adjali, L., et al. 2010, *Proc. SPIE*, 7735, 773508
 Becker, A. 2015, HOTPANTS: High Order Transform of PSF AND Template Subtraction, Astrophysics Source Code Library, ascl:1504.004
 Bellm, E. C., Kulkarni, S. R., Graham, M. J., et al. 2019, *PASP*, 131, 018002
 Bernstein, R., Shethman, S. A., Gunnels, S. M., Mochnacki, S., & Athey, A. E. 2003, *Proc. SPIE*, 4841, 1694
 Bersten, M. C., Benvenuto, O., & Hamuy, M. 2011, *ApJ*, 729, 61
 Bersten, M. C., Folatelli, G., García, F., et al. 2018, *Natur*, 554, 497
 Blondin, S., & Tonry, J. L. 2007, *ApJ*, 666, 1024
 Bose, S., Dong, S., Kochanek, C. S., et al. 2020, arXiv:2007.00008
 Bostroem, K. A., Valenti, S., Horesh, A., et al. 2019, *MNRAS*, 485, 5120
 Bostroem, K. A., Valenti, S., Sand, D. J., et al. 2020, *ApJ*, 895, 31
 Breeveld, A. A., Landsman, W., Holland, S. T., et al. 2011, in AIP Conf. Ser. 1358, Gamma-Ray Bursts 2010, ed. J. E. McEnery, J. L. Racusin, & N. Gehrels (Melville, NY: AIP), 373
 Brown, P. J., Breeveld, A. A., Holland, S., Kuin, P., & Pritchard, T. 2014, *Ap&SS*, 354, 89
 Brown, P. J., Holland, S. T., Immler, S., et al. 2009, *AJ*, 137, 4517
 Brown, T. M., Baliber, N., Bianco, F. B., et al. 2013, *PASP*, 125, 1031
 Cardelli, J. A., Clayton, G. C., & Mathis, J. S. 1989, *ApJ*, 345, 245
 Chevalier, R. A., & Fransson, C. 1994, *ApJ*, 420, 268
 Chugai, N. N., Chevalier, R. A., & Utrobin, V. P. 2007, *ApJ*, 662, 1136
 Czerny, B., Beaton, R., Bejger, M., et al. 2018, *SSRv*, 214, 32
 Davies, B., & Beasor, E. R. 2018, *MNRAS*, 474, 2116
 Davies, B., & Beasor, E. R. 2020, *MNRAS*, 496, L142
 Davis, S., Hsiao, E. Y., Ashall, C., et al. 2019, *ApJ*, 887, 4
 de Jaeger, T., Anderson, J. P., Galbany, L., et al. 2018, *MNRAS*, 476, 4592
 Dessart, L., & Hillier, D. J. 2005, *A&A*, 439, 671
 Eikenberry, S., Elston, R., Raines, S. N., et al. 2006, *Proc. SPIE*, 6269, 626917
 Ekström, S., Georgy, C., Eggenberger, P., et al. 2012, *A&A*, 537, A146
 Faran, T., Poznanski, D., Filippenko, A. V., et al. 2014, *MNRAS*, 442, 844
 Foreman-Mackey, D., Hogg, D. W., Lang, D., & Goodman, J. 2013, *PASP*, 125, 306
 Freudling, W., Romaniello, M., Bramich, D. M., et al. 2013, *A&A*, 559, A96
 Fuller, J. 2017, *MNRAS*, 470, 1642
 Galbany, L., Anderson, J. P., Rosales-Ortega, F. F., et al. 2016a, *MNRAS*, 455, 4087
 Galbany, L., Anderson, J. P., Sánchez, S. F., et al. 2018, *ApJ*, 855, 107
 Galbany, L., Hamuy, M., Phillips, M. M., et al. 2016b, *AJ*, 151, 33
 Gall, C., Hjorth, J., Watson, D., et al. 2014, *Natur*, 511, 326
 Gehrels, N., Chincarini, G., Giommi, P., et al. 2004, *ApJ*, 611, 1005
 Gimeno, G., Roth, K., Chiboucas, K., et al. 2016, *Proc. SPIE*, 9908, 872
 Goldberg, J. A., & Bildsten, L. 2020, *ApJL*, 895, L45

- Goldberg, J. A., Bildsten, L., & Paxton, B. 2019, *ApJ*, **879**, 3
- Gutiérrez, C. P., Anderson, J. P., Hamuy, M., et al. 2017, *ApJ*, **850**, 89
- Hamuy, M., Pinto, P. A., Maza, J., et al. 2001, *ApJ*, **558**, 615
- Heger, A., Fryer, C. L., Woosley, S. E., Langer, N., & Hartmann, D. H. 2003, *ApJ*, **591**, 288
- Hook, I. M., Jørgensen, I., Allington-Smith, J. R., et al. 2004, *PASP*, **116**, 425
- Horiuchi, S., Nakamura, K., Takiwaki, T., Kotake, K., & Tanaka, M. 2014, *MNRAS*, **445**, L99
- Hosseinzadeh, G. 2020, griffin-h/lightcurve_fitting v0.1.0, Zenodo, doi:10.5281/zenodo.3908580
- Hosseinzadeh, G., Valenti, S., McCully, C., et al. 2018, *ApJ*, **861**, 63
- Hsiao, E. Y., Phillips, M. M., Marion, G. H., et al. 2019, *PASP*, **131**, 014002
- Hunter, J. D. 2007, *CSE*, **9**, 90
- Insera, C., Turatto, M., Pastorello, A., et al. 2012, *MNRAS*, **422**, 1122
- Jerkstrand, A., Ertl, T., Janka, H. T., et al. 2018, *MNRAS*, **475**, 277
- Jerkstrand, A., Fransson, C., & Kozma, C. 2011, *A&A*, **530**, A45
- Jerkstrand, A., Fransson, C., Maguire, K., et al. 2012, *A&A*, **546**, A28
- Jerkstrand, A., Smartt, S. J., Fraser, M., et al. 2014, *MNRAS*, **439**, 3694
- Jha, S. 2018, Transient Name Server Classification Report, 2018-884, 1
- Jones, M. I., Hamuy, M., Lira, P., et al. 2009, *ApJ*, **696**, 1176
- Kasen, D., & Woosley, S. E. 2009, *ApJ*, **703**, 2205
- Kennicutt, R. C. J. 1998, *ApJ*, **498**, 541
- Kirshner, R. P., & Kwan, J. 1974, *ApJ*, **193**, 27
- Kochanek, C. S., Khan, R., & Dai, X. 2012, *ApJ*, **759**, 20
- Kochanek, C. S., Shappee, B. J., Stanek, K. Z., et al. 2017, *PASP*, **129**, 104502
- Leonard, D. C., Filippenko, A. V., Gates, E. L., et al. 2002a, *PASP*, **114**, 35
- Leonard, D. C., Filippenko, A. V., Li, W., et al. 2002b, *AJ*, **124**, 2490
- Li, W., Leaman, J., Chornock, R., et al. 2011, *MNRAS*, **412**, 1441
- Lupton, R. H., Jurić, M., Ivezić, Z., et al. 2005, AAS Meeting, **207**, 133.08
- Martinez, L., & Bersten, M. C. 2019, *A&A*, **629**, A124
- Martinez, L., Bersten, M. C., Anderson, J. P., et al. 2020, *A&A*, **642**, A143
- Mathewson, D. S., Ford, V. L., & Buchhorn, M. 1992, *ApJS*, **81**, 413
- Mauerhan, J., & Smith, N. 2012, *MNRAS*, **424**, 2659
- McKinney, W. 2010, in Proc. 9th Python in Science Conf., ed. S. van der Walt & J. Millman, 56, doi:10.25080/Majora-92bf1922-00a
- Morozova, V., Piro, A. L., Fuller, J., & van Dyk, S. D. 2020, *ApJL*, **891**, L32
- Morozova, V., Piro, A. L., Renzo, M., et al. 2015, *ApJ*, **814**, 63
- Morozova, V., Piro, A. L., & Valenti, S. 2017, *ApJ*, **838**, 28
- Morozova, V., Piro, A. L., & Valenti, S. 2018, *ApJ*, **858**, 15
- Müller, T., Prieto, J. L., Pejcha, O., & Clocchiatti, A. 2017, *ApJ*, **841**, 127
- Munari, U., & Zwitter, T. 1997, *A&A*, **318**, 269
- Nakaoka, T., Kawabata, K. S., Maeda, K., et al. 2018, *ApJ*, **859**, 78
- Olivares, E. F., Hamuy, M., Pignata, G., et al. 2010, *ApJ*, **715**, 833
- Osterbrock, D. E., & Ferland, G. J. 2006, *Astrophysics of Gaseous Nebulae and Active Galactic Nuclei* (2nd ed.; Sausalito, CA: Univ. Science Books)
- Ouchi, R., & Maeda, K. 2019, *ApJ*, **877**, 92
- Pastorello, A., Sauer, D., Taubenberger, S., et al. 2006, *MNRAS*, **370**, 1752
- Paxton, B., Schwab, J., Bauer, E. B., et al. 2018, *ApJS*, **234**, 34
- Pettini, M., & Pagel, B. E. J. 2004, *MNRAS*, **348**, L59
- Phillips, M. M., Simon, J. D., Morrell, N., et al. 2013, *ApJ*, **779**, 38
- Piro, A. L., Muhleisen, M., Arcavi, I., et al. 2017, *ApJ*, **846**, 94
- Poznanski, D., Nugent, P. E., & Filippenko, A. V. 2010, *ApJ*, **721**, 956
- Poznanski, D., Prochaska, J. X., & Bloom, J. S. 2012, *MNRAS*, **426**, 1465
- Quataert, E., & Shiode, J. 2012, *MNRAS*, **423**, L92
- Rabinak, I., & Waxman, E. 2011, *ApJ*, **728**, 63
- Reichart, D., Nysewander, M., Moran, J., et al. 2005, *NCimC*, **28**, 767
- Rui, L., Wang, X., Mo, J., et al. 2019, *MNRAS*, **485**, 1990
- Sapir, N., & Waxman, E. 2017, *ApJ*, **838**, 130
- Savitzky, A., & Golay, M. J. E. 1964, *AnaCh*, **36**, 1627
- Schlaflly, E. F., & Finkbeiner, D. P. 2011, *ApJ*, **737**, 103
- Schmelling, M. 1995, *PhyS*, **51**, 676
- Shappee, B. J., Prieto, J. L., Grupe, D., et al. 2014, *ApJ*, **788**, 48
- Simcoe, R. A., Burgasser, A. J., Schechter, P. L., et al. 2013, *PASP*, **125**, 270
- Smartt, S. J. 2015, *PASA*, **32**, e016
- Smartt, S. J., Eldridge, J. J., Crockett, R. M., & Maund, J. R. 2009, *MNRAS*, **395**, 1409
- Smith, K. W., Smartt, S. J., Young, D. R., et al. 2020, *PASP*, **132**, 085002
- Smith, N. 2014, *ARA&A*, **52**, 487
- Smith, N., & Arnett, W. D. 2014, *ApJ*, **785**, 82
- Spiro, S., Pastorello, A., Pumo, M. L., et al. 2014, *MNRAS*, **439**, 2873
- Sukhbold, T., Ertl, T., Woosley, S. E., Brown, J. M., & Janka, H. T. 2016, *ApJ*, **821**, 38
- Takáts, K., Pignata, G., Pumo, M. L., et al. 2015, *MNRAS*, **450**, 3137
- Tartaglia, L., Sand, D. J., Valenti, S., et al. 2018, *ApJ*, **853**, 62
- Tomasella, L., Cappellaro, E., Fraser, M., et al. 2013, *MNRAS*, **434**, 1636
- Tonry, J. L. 2011, *PASP*, **123**, 58
- Utrobin, V. P., & Chugai, N. N. 2015, *A&A*, **575**, A100
- Utrobin, V. P., & Chugai, N. N. 2017, *MNRAS*, **472**, 5004
- Valenti, S., Benetti, S., Cappellaro, E., et al. 2008, *MNRAS*, **383**, 1485
- Valenti, S., Howell, D. A., Stritzinger, M. D., et al. 2016, *MNRAS*, **459**, 3939
- Valenti, S., Sand, D., Pastorello, A., et al. 2014, *MNRAS*, **438**, L101
- Valenti, S., Sand, D. J., & Wyatt, S. 2018, Transient Name Server Discovery Report, 2018-876, 1
- van Dyk, S. D., Li, W., & Filippenko, A. V. 2003, *PASP*, **115**, 1
- Walmswell, J. J., & Eldridge, J. J. 2012, *MNRAS*, **419**, 2054
- Willeck, J. A., Courteau, S., Faber, S. M., et al. 1997, *ApJS*, **109**, 333
- Woosley, S. E., & Heger, A. 2007, *PhR*, **442**, 269
- Yang, S., Sand, D. J., Valenti, S., et al. 2019, *ApJ*, **875**, 59
- Yang, S., Valenti, S., Cappellaro, E., et al. 2017, *ApJL*, **851**, L48
- Yaron, O., & Gal-Yam, A. 2012, *PASP*, **124**, 668
- Yaron, O., Perley, D. A., Gal-Yam, A., et al. 2017, *NatPh*, **13**, 510